2018

Effect of Stainless Steel and Titanium Corrosion on CFRP Structural Integrity

Daniel C. Danckert
University of Rhode Island, dan289uri@gmail.com

EFFECT OF STAINLESS STEEL AND TITANIUM CORROSION ON CFRP STRUCTURAL INTEGRITY

BY

DANIEL C. DANCKERT

A THESIS SUBMITTED IN PARTIAL FULFILLMENT OF THE

REQUIREMENTS FOR THE DEGREE OF

MASTER OF SCIENCE

IN

CHEMICAL ENGINEERING

UNIVERSITY OF RHODE ISLAND

2018

MASTER OF SCIENCE THESIS

OF

DANIEL C. DANCKERT

APPROVED:

Thesis Committee:

Major Professor Richard Brown

Samantha Meenach

Leon Thiem

Nasser H. Zawia
DEAN OF THE GRADUATE SCHOOL

UNIVERSITY OF RHODE ISLAND
2018

ABSTRACT

In this study, carbon fiber reinforced polymer (CFRP) was connected to either a stainless steel or titanium screw and then placed in a salt water solution, with measurements being taken using a potentiostatic electrochemical impedance spectroscopy (PEIS) system to determine each system's impedance values at varying frequencies. The collected numerical data was then used to determine the number of interfaces within each sample via a modeling program in the PEIS system that used Randles Circuits (RC) in series. Samples were also examined using a scanning electron microscope (SEM) and an energy-dispersive X-ray spectroscopy (EDS) system to determine if any products of the metallic corrosion had caused any mechanical damage to the CFRP. It was noted that the titanium exhibited stable impedance values over the course of the experiment while also not causing any damage to the CFRP structure. The stainless steel on the other hand exhibited more erratic impedance values of the course of the study while also showing apparent damage to the surface of the CFRP to which it was connected in the form of delamination.

KEYWORDS

Crevice corrosion, pitting corrosion, galvanic corrosion, carbon fiber reinforced polymer (CFRP), stainless steel, titanium, potentiostatic electrochemical impedance spectroscopy (PEIS), mechanical damage

ACKNOWLEDGMENTS

I would firstly like to thank my advisor and major professor, Dr. Richard Brown for his guidance and support throughout this process. This thesis has taken a great deal of time and effort, and without Dr. Brown's support, I would never have arrived at this point. I would also like to thank Dr. Samantha Meenach and Dr. Leon Thiem for their assistance and for serving as members of my master's committee, and for Dr. Sigrid Berka for agreeing to chair my thesis defense committee. In addition, I would like to thank Mr. Michael Platek of the Sensors and Surface Technology (SST) laboratory for his assistance with analyzing the various samples under the SST lab's Scanning Electron Microscope.

I would also like to extend my sincere thanks to my lab partner, Jordan A. Ortiz. Your assistance, collaboration, and insights in the experimental and data analysis portion of this process was invaluable to the efforts of completing this thesis.

Lastly, I would like to thank my fiancée, Maria. Your unwavering support for me during the pursuit of my master's degree, whether it be by being flexible with our schedule so that I could perform the necessary work to complete this thesis or by giving me the motivation to push through when my reserves were near depletion, you are a major reason why this thesis exists.

TABLE OF CONTENTS

LIST OF TABLES

LIST OF FIGURES

CHAPTER 1

INTRODUCTION

For many years, stainless steel and titanium have been used as building materials in marine environments, with stainless steel being the more prevalent material due to its relatively lower cost. With the advent of more advanced construction materials such as carbon fiber reinforced polymer (CFRP), stainless steel and titanium structures are increasingly coming into contact with CFRP, which could affect their corrosion behavior (Commander 1999).

Due to the near ubiquitous use of stainless steel in construction, both in marine and non-marine settings, the corrosion mechanisms of this material are well understood (Tsutsumi et al. 2007; Smiderle et al. 2014). While titanium has not been used for construction as frequently as stainless steel due to its higher relative cost, its corrosion mechanism are also reasonably well understood in that titanium is known to create a stable passivating layer when exposed to a corrosive environment such as salt water (El-Dahshan et al. 2002; Rebak 2013). Extensive study has also already been allotted to the effect that CFRP has on the corrosion rates of metals (Tucker and Brown 1989; Tucker et al. 1990). Fewer studies however have been performed on how the corrosion of metals affects CFRP structures, particularly how the corrosion of metals affects the structural integrity of CFRP, and herein lies the gap in knowledge. With the growing prevalence of CFRP in marine applications, such as that found in the catamarans being raced in the America's Cup (Commander 1999), there exists an

increasing likelihood of CFRP coupled to stainless steel or titanium components being used to construct these and similar vessels. This study aims to better quantify if the corrosion of metals, specifically stainless steel and titanium in the case of this study, in the presence of salt water has any adverse effects on the structural integrity of Carbon Fiber Reinforced Polymer (CFRP) when the two different materials are in direct contact with one another.

CHAPTER 2

REVIEW OF LITERATURE

This section reviews studies concerning what is already known and has already been studied regarding corrosion of CFRP, stainless steel, and titanium in salt water, as well as how CFRP affects the corrosion of stainless steel and titanium in the presence of salt water. This section will not however discuss how stainless steel and titanium corrosion affect the structural integrity of CFRP in a salt water environment because, after an extensive literature search, no such study was found.

CORROSION OF THE INDIVIDUAL MATERIALS

The corrosion mechanisms and rates of the three materials used in this study – stainless steel, titanium, and CFRP – have all be thoroughly researched in previous studies. This means that corrosion phenomena surrounding these three materials individually are well understood. The following three sections detail some of the studies that have been performed to support this statement.

CFRP

In the case of CFRP, a study by Brown and Reynolds was performed to investigate the effects of three different chloride salt solutions on the corrosion of CFRP. In the case of the 3.5wt% NaCl solution that was used in a portion of that study, surface condition of the CFRP samples after a length of time was visually observed via a Scanning Electron Microscope (SEM). In addition to this, the

corrosion rate was able to be determined via measurements taken using potentiodynamic electrochemical impedance spectroscopy (PEIS). The visual and quantitative data obtained in this study detailed the damage to the surface of the CFRP samples that had been exposed to the NaCl solution, with the quantitative PEIS data being used to determine the corrosion rate of the material, which could, with additional study, be potentially used to create a model to predict material failure based on the gathered data (Brown and Reynolds 1995).

While the authors of this study did not go into detail as to what kind of damage was found on the surface of the samples, as their main focus was whether different chloride salt solutions would affect CFRP differently, the authors did site previous studies performed by Chen and Skerry (Chen and Skerry 1991), Alias and Brown (Alias and Brown 1992), Kaushik, Alias, and Brown (Kaushik et al. 1991), and a follow-up study by Alias and Brown (Alias and Brown 1995) in which varying types of damage were observed on the surface of the CFRP, to include uniform dissolution of the polymer structure, stripping of the polymer structure, and localized damage such as osmotically driven blistering (Brown and Reynolds 1995). In addition to this, the data obtained from the PEIS seemed to indicate when damage to the CFRP surface was occurring, namely that the damage was occurring at the points when there was an observed decrease in both the measured impedance values as well as the measured phase angle values (Brown and Reynolds 1995). The data was also used to create a model for predicting the corrosion behavior of CFRP in salt water over time in that the most significant change occurred within the first seven days of the samples' lives and that PEIS modeling showed that only one Randle Circuit (RC) was required to be able

to successfully model the data, thereby indicating that only one corrosion interface was present in the system (Brown and Reynolds 1995).

In a subsequent study performed by Qin, Brown, Ghiorse, and Shuford, the authors sought to determine whether or not the type of fiber used in the CFRP matrix would have any effect on the mechanism or form of the corrosion damage when the CFRP was subjected to a salt water environment (Qin et al. 1995). As with the previously-mentioned paper, this study also used SEM and PEIS to evaluate the samples, in addition to other methods. When reviewing the samples via SEM that had exposed directly to the salt water solution, cracking was observed as well as regions of bare carbon fibers where the adhesive polymer had previously existed. This state was found across all of the sample independent of the type of fiber used. The authors theorized that the cracking could have come from increase in osmotic pressure due to the formation of hydroxyl ions via the reaction with oxygen in the water at the now charged interface of the CFRP's surface (Qin et al. 1995). This increase in pressure could have led to the cracking observed on the samples' surfaces. Additionally, the increase in the osmotic pressure could have created a scenario in which in the increased pressure also increased the stress on the polymer to the point where that stress exceeded the yield stress, thereby causing the crack and delaminate (Qin et al. 1995).

As with the previous study, the PEIS values were found to also be used to determine when the material could potentially fail, based on the fall in both the measured impedance values as well as the measurement phase angle values.

In a third study, MacAnder and Silvergleit reviewed the effect of adding stress, primarily in the form of static and fatigue stress, on the performance of CFRP in a salt water environment (MacAnder and Silvergleit 1977). While this particular study did not focus on how the salt water environment affected the corrosion of the CFRP samples, it did however discuss how immersion of CFRP samples in salt water affected the strength of the samples as a function of time, that is how the structural integrity of the CFRP can be changed by immersion in salt water. The researchers found that CFRP samples that were immersed in water for 12-26 months exhibited a lower shear strength value than the dry samples, although this was dependent on the void content of the particular CFRP structure as the CFRP that were more compact did not exhibit the same changes as the samples that could absorb more water (MacAnder and Silvergleit 1977). In all, the importance of this study is that it was shown that CFRP's structural integrity can be affected by salt water, meaning that it could potentially be further affected the salt water corrosion products of stainless steel and titanium.

STAINLESS STEEL

One study performed by Ahmad and Malik focused on the corrosion behavior of 9 different types of stainless steels, both of the conventional and high alloy variety, in unchlorinated or chlorinated Arabian Gulf seawater at either 25°C or 50°C (Ahmad and Malik 2001). In this particular study, the researchers used potentiodynamic cyclic polarization to quantify the corrosion rate of each sample setup. The researchers found that the high alloy stainless steels, specifically 3127 hMO, 1925 hMO, 254 SMO, 625 SMO, and Remanit-4565 did not readily exhibit crevice or

pitting corrosion in any of the sample setups (Ahmad and Malik 2001). The more common varieties of stainless steel, specifically the 316L and 317L, exhibited very poor corrosion resistance in both the unchlorinated and chlorinated water as well as at both temperature settings. The 316L and 317L stainless steel samples exhibited a high breakdown potential (E_b) value as well as higher measured maximum current densities (I_{max}) when compared to the high alloyed stainless steels, meaning that these samples were corroding more readily (Ahmad and Malik 2001). Despite this indication in the data, the researchers did not visually examine the samples, meaning that they could not determine which corrosion mechanisms were present. The other two steel specimens used, 904L and duplex 2205, exhibited mixed results, with moderate corrosion resistance being seen at 25°C and poor corrosion resistance being observed at 50°C (Ahmad and Malik 2001). The highlight of this study was the usage of different types of stainless steel and the indication that a particular stainless steel type can have good or poor corrosion resistance depending on the alloying components of a particular stainless steel.

The next study, performed by Tsutsumi, Nishikata, and Tsuru sharpened the focus of what was covered in the study performed by Ahmad and Malik. The researchers sought to quantify the pitting corrosion mechanism in 304 stainless steel (304SS) when drops of magnesium chloride ($MgCl_2$) were placed on the surface of a 304SS sample with the end goal being to clarify the rusting mechanism in marine atmospheres (Tsutsumi et al. 2007). While actual seawater contains several different kinds of chloride salts, $MgCl_2$ was chosen as the sole chloride salt to be used to simplify the pitting corrosion phenomena. Based on their testing, the researchers

made three observation regarding the propagation of pitting corrosion of the surface of 304SS. The first observation was that the size of the pit observed was relative to the size of the $MgCl_2$ droplet, with overall larger droplets exhibiting larger pits. The second observation noted the importance of the critical relative humidity (RH) for the chloride concentration in the formation of pits. The researchers noticed that pitting occurred most regularly at RH values between 55% and 75% (8.5M and 4.9M) in a moderately acidic environment (pH = 4 to 7). They also noted that the RH was a more significant contributing factor, as uniform pitting corrosion was still present at pH values below 4 as long as the RH values were high enough (Tsutsumi et al. 2007). The third observation made by the researchers dealt with the geometry of the pits. The researchers used a laser microscope to measure the diameter and depth of the pits formed during the corrosion process. They noticed that the pits being formed were relatively shallow, leading them to theorize that the pit propagated preferentially in a horizontal direction relative to the surface of the 304SS (Tsutsumi et al. 2007). The significance of this study was a focused review of one type of stainless steel being subjected to one type of corrosion mechanism, and then reviewing the behavior of that corrosion mechanism.

The final study reviewed for stainless steel was performed by Elsariti and Haftirman, in which they reviewed stress corrosion cracking for austenitic stainless steels in sodium chloride solutions. Like the previous study reviewed, this particular study focused on one specific corrosion mechanism, namely stress corrosion cracking (SCC). This study also focused on one specific family of austenitic stainless steels, type 316SS. The researchers applied a constant load of 90% yield strength to the

316SS submerged the samples in one of two NaCl solutions at room temperature. The first solution had a NaCl concentration of 3.5wt% while the second had a concentration of 9.35wt% (Elsariti and Haftirman 2013). The researchers found that, at 3.5wt% concentration NaCl in a shorter span of time (less than 838 hours), no cracking was found. The researchers noted that this was consistent with published data that had been reviewed and they theorized that a longer residence would be required to allow the corrosion mechanism to take hold and propagate in the 3.5wt% system. This was later confirmed when SCC was found in samples that were submerged to 1,244 hours and 1,678 hours. The researchers did however observe cracks at 838 hours of residence time in the 9.35wt% NaCl solution, indicating that SCC of 316SS was highly sensitive to NaCl concentration (Elsariti and Haftirman 2013).

TITANIUM

The first document related to titanium that was reviewed was unlike the previous ones reviewed in this study in that it was not a research paper but was rather a chapter from a book detailing the corrosion of non-ferrous alloys. In this chapter, the author, Raul B. Rebak, discusses how titanium has "outstanding" corrosion resistance when faced with a variety of organic and inorganic corrosion media, which includes seawater (Rebak 2013). Rebak stated that this was due to the extremely stable oxide layer that titanium formed when confronted by these corrosion media, citing the book "Atlas of Electrochemical Equilibria in Aqueous Solutions" written by Marcel Pourbaix in 1974. Rebak further discussed general corrosion characteristics of

titanium, making note that different grades of titanium have different corrosion resistance characteristics. One of the most common commercially available titanium alloys, Titanium Grade 2 (also called commercially pure titanium), has good corrosion resistance and is used in different applications where corrosion resistance is required. It is not however the most corrosion resistant titanium alloy, as for example Grade 7 (Grade 2 with the addition of palladium) has much better corrosion resistance. Grade 7 is also however much more expensive than Grade 2, and is therefore not well suited for applications where cost-savings is a primary concern. Grade 12 titanium (Grade 2 with molybdenum and nickel added) is another alloy that has better corrosion resistance than Grade 2 but is less expensive than Grade 7. The point of mentioning the different types of titanium alloys and their different corrosion properties is the same as why the different corrosion characteristics of different stainless steel alloys was discussed: different corrosion characteristics can be achieved for a material depending on the alloying elements within the material, but this increased performance comes at an increased price. Give these two elements, a compromise must be reached based on the application requirements.

Another point that Rebak makes regarding the corrosion behavior of titanium is the dependence of the media to which it is subjected, as well as environmental conditions such as temperature (Rebak 2013). Rebak specifically focuses on reducing acids, with a specific focus on sulfuric acid, noting that acid concentration, impurities within the acid, and the temperature of the acid play a role in the corrosion-resisting performance of the titanium alloy.

The final aspect of titanium corrosion that Rebak covers is the localized corrosion that titanium alloys are mainly susceptible to, namely crevice corrosion and environmental-assisted cracking (SSC and hydrogen embrittlement) (Rebak 2013). Titanium is known to exhibit crevice corrosion in solutions containing sulfates, chlorides, and other halides, with higher temperatures and concentrations of the anion making the titanium alloy more susceptible to crevice corrosion, which Rebak noted had been investigated with studies performed by McKay and Mitton in 1985 and by Schutz in 1991. This crevice corrosion phenomena, Rebak stated, was due to the creation of a highly acidic area where crevice corrosion could occur, which was investigated in a study performed by Griess in 1968. Rebak also noted that titanium alloys could exhibit SCC in low molecular weight alcohols, with intergranular and transgranular forms of SCC being observed (Rebak 2013). Given this fact, Rebak notes that titanium is resistant to SCC in chloride solutions such as salt water and is resistant to corrosion in seawater.

The first study reviewed was a report that came from Judy and Goode, in which these researchers investigated SCC characteristics of titanium alloys in salt water as part of a project for the United States Navy (Judy Jr. and Goode 1967). In their experiments, the researchers used the precracked-cantilever-beam test method in which a titanium test bar with a fatigue-crack flaw was bent with a specified amount of pressure in a 3.5wt% NaCl solution. This load stress, also known as the stress intensity factor, designated by the researchers as K_I, was calculated using the following equation:

$$K_I = \frac{4.12\ M\sqrt{\frac{1}{\alpha^{\epsilon}} - \alpha^{j}}}{BD^{3/2}};\ \alpha \equiv 1 - \frac{a}{D}; \qquad (1)$$

in which *B* and *D* represented the width and height of the sample, respectively, *M* represents the angle of the fatigue crack flaw, ε corresponds to the crack depth, and *a* is the effective crack length. The authors did not explain what the *j* exponent above the α coefficient represented. The initial calculated K_I level was denoted as "No Break" (Judy Jr. and Goode 1967). This equation was used to calculate the threshold stress intensity factor for SCC, K_{Issc}, which could then be compared to the stress intensity required to fracture in air, K_{Ix}, to give an indication as to the alloy's resistance to SCC.

In their results, the researchers found that the SCC data did not show a direct correlation to the mechanical properties of the material, of which they specifically listed yield strength, drop weight tear energy, and Charpy V-notch test energy (Judy Jr. and Goode 1967). They noted that all of the alloys showed varying degrees of susceptibility to SCC, with the sensitivity of some titanium alloys being very slight, particularly when that titanium alloy included some molybdenum in its chemical makeup. As with the book chapter prepared by Rebak, this study also stressed that the alloying elements within the titanium alloy have a significant effect on the corrosion resistance of titanium alloy.

The final titanium study reviewed was performed by El-Dahshan, Shams El Din, and Haggag and focused on galvanic corrosion for titanium when coupled with aluminum (Al) brass in Arabian Gulf seawater (El-Dahshan et al. 2002). The researchers also ran tests with 316L stainless steel and Al brass coupled together but for the purposes of this review, only the results of the Titanium-Al brass combination will be reviewed. The researchers first reviewed the open circuit potential (OCP) of

the individual metals, with titanium be examined at 25°C in stagnant seawater. Based on the measured OCP values, which started with negative values and gradually moved toward less negative values, the researchers surmised that the titanium sample was quickly forming a passive film layer on the sample surface. The OCP values that the researchers obtained appeared to be in-line with those of literature that they reviewed (El-Dahshan et al. 2002). The titanium OCP values were then compared to the measured OCP values of the Al brass, of which there was a difference of several hundred millivolts. The researchers theorized that, based on the difference in OCP values, there would exist a scenario where a galvanic cell would readily occur when titanium and Al brass were coupled together. This was confirmed in later testing, in which the individual titanium and Al brass pieces were short circuited once a steady corrosion potential for each had been established. After this, the OCP of the now coupled metals was observed as a function of time. It was noted that, after 10-20hrs, the OCP values measured at the Al brass sample tended towards less negative values, indicating the formation of a passivating film (El-Dahshan et al. 2002). After longer periods of time (250-350 hrs.), the researchers noted that the corrosion currents for the system decreased as a function of time, which they attributed to the build-up of calcium carbonate precipitate on the surface of the cathode (titanium) and partly on the anode (Al brass), the calcium carbonate being a product of the reduction of O_2 forced by the galvanic cell at the cathode's surface via the following two reactions:

$$O_2 + 2H_2O + 4e^- \rightleftharpoons 4OH^-;$$

$$HCO_3^- + OH^- \rightleftharpoons CO_3^{2-} + H_2O;$$

in which the calcium ion in the seawater was precipitated out of the seawater by the newly formed carbonate ion. It was theorized by the researchers that, if the

concentration of O2 was reduced, then the formation of $CaCO_3$ would be hindered, thereby reducing the galvanic corrosion of the Al brass.

INDUCED CORROSION OF METALS BY CFRP

It is well understood how an interaction between metals and CFRP will affect the corrosion mechanisms of metals, specifically how CFRP will induce metals to corrode more readily in the presence of salt water (Tucker et al. 1990). This is due to the relationship between the majority of commonly used metals and CFRP on the galvanic series table, seen in *Figure 1*. As seen on this table, CFRP (represented in this case by graphite, a close analog) is significantly nobler than stainless steel and noticeably nobler than titanium. When either of these two metals are attached directly to CFRP in the presence of salt water, a galvanic cell is created in which the CFRP acts as the cathode, the metal acts as the anode, and the salt water is a medium through which the electric current can flow. This galvanic cell leads to preferential corrosion of the anode, which is a process that has been well studied and documented (Tucker et al. 1990).

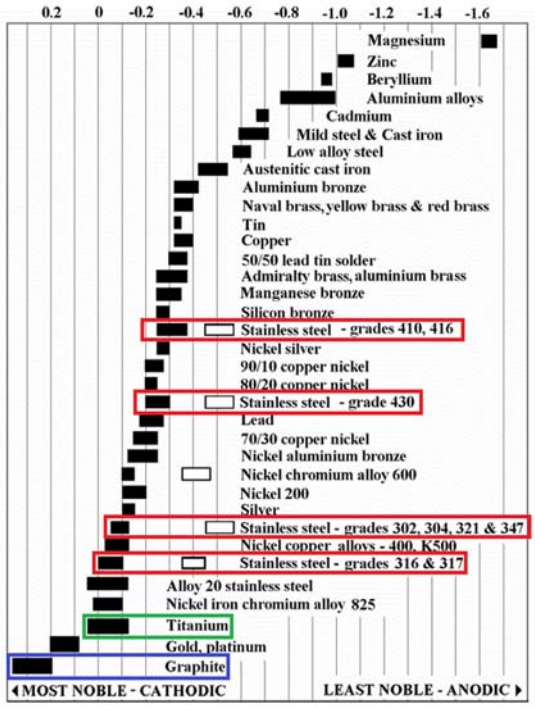

Figure 1: Galvanic series in seawater table detailing the relationship between CFRP (represented by Graphite, **BLUE**) and the two metals used in this study, Titanium (**GREEN**) and Stainless Steel (**RED**) in terms of cathodic and anodic potential. The greater the distance between the two materials, the greater the driving force behind the galvanic corrosion (SSINA KnowledgeBase).

The first study reviewed came from Tucker, Brown, and Russell, in which CFRP coupled directly with 5 different metals in natural seawater: 2014 bare aluminum, 2014 hard-anodized aluminum, pure-grade titanium, 316 stainless steel, and Monel (Tucker et al. 1990). For the purposes of this review, only the testing and results related to the titanium and the 316 stainless steel (316SS) samples were reviewed. For testing, the researchers placed coupled samples in a tank in a lab maintained at 70±10°F. The seawater used came from Narragansett Bay and was changed weekly in order to maintain the salinity content. In conjunction with these samples, additional coupled samples were suspended in nets and immersed directly into Narragansett Bay at the University of Rhode Island's Bay Campus. This allowed the researchers to take into account environmental factors that could not easily be replicated in a laboratory setting. The exposure time for all samples was approximately six months. Additionally, control samples of each metal were included in separate tanks and in separate nets at each setup (Tucker et al. 1990).

After the 6 months elapsed, the researchers noted that no corrosion was evident on the titanium samples in either the laboratory setup or the Narragansett Bay setup. Additionally, none of the CFRP samples to which the titanium samples had been coupled showed any signs of degradation. The only noticeable change that the researchers could observe was a slight discoloration on the surface of the titanium. The researchers theorized that this was due to the creation of a passivating film, in the case of the laboratory samples, and marine growth, in the case of the Narragansett Bay samples (Tucker et al. 1990). The 316SS samples however didn't fare as well. The researchers observed that, after a very short amount of time, rust could be seen on the laboratory samples at both the interface region been the 316SS and the CFRP as well as the contact region. It was later determined through more thorough visual analysis that crevice corrosion was the mechanism in this system. The Narragansett Bay samples also exhibited visible crevice corrosion along the surface of the 316SS, although there was not a significant build-up of corrosion product, a fact that the researchers attributed to the constant movement of Narragansett Bay seawater. When the CFRP portion of the coupled samples was visually analyzed, no blistering or other form of degradation was evident. The researchers did find crystalline deposits on the surface of the CFRP sample in the laboratory setup where the composite had been exposed to seawater (Tucker et al. 1990). The researchers stated that this had been determined in a previous 1988 study by Tucker to be aragonite. A similar crystalline build-up on the Narragansett Bay samples was not observed due to the marine growth found on the samples.

Another study by Tucker and Brown focused on how the CFRP could be affected by galvanically-coupled mild steel, specifically on the formation of blisters within the CRFP structure as a result of the galvanic coupling (Tucker and Brown 1989). It should be noted that, while Tucker and Brown's study sounds similar to the premise of this study, Tucker and Brown did not focus on how the corrosion product of the coupled material could affect the structural integrity of the CFRP.

In this study, a total of 4 time periods was used as the resident times during which the samples were soaked in filtered seawater from Narragansett Bay: one week, one month, three months, and six months. Two different types of CFRP were used for the testing in this study, and a total of 5 samples from each type of CFRP were subjected to strain in the form of a three-point bend before being immersed into the seawater. An identical number of samples were also placed into a different tank of seawater with the same environmental control settings, with the only difference being that these samples had not been placed in a three-point bend apparatus prior to be immersed in the seawater (Tucker and Brown 1989).

After being removed from the seawater, the CFRP samples were weighted. Tucker and Brown noted that the CFRP samples exhibited weight gains, which they attributed to the formation of aragonite crystals on the surface of the CFRP samples. Additionally, the researchers noticed the formation of blisters on the surface of the CFRP that had been coupled with the mild steel and immersed in seawater. CFRP samples on the other hand that had not been coupled with mild steel did not exhibit any crystal growth or blistering.

CHAPTER 3

METHODOLOGY

Testing and analysis consisted of two portions: a quantitative portion to obtain numerical data for analysis and a qualitative portion mainly in the form visual analysis of the tested samples. The thought process was to use the qualitative portion of the data to substantiate, or disprove, the hypothesis of this experiment and then use the quantitative data to determine whether or not the onset of the hypothesized condition can be detected prior to catastrophic failure of the CFRP.

SAMPLE PREPARATION

For the quantitative portion, a stainless steel screw or a titanium screw with 10-24 threads was inserted into a CFRP sheet, approximately 0.146-inch-thick, sectioned to a size of approximately 1⅝-inch-wide by 1⅛-inch-long rectangles. The CFRP sheet was drilled and tapped in the center of the sheet to enable the screw to be inserted without creating a preloaded stress on the CFRP sheet. The screws used for these experiments were machine screws purchased from a local hardware store and the CFRP polymer slabs were obtained from a previous experiment, of which the source was proprietary. A piece of PVC pipe measuring approximately 0.8 inch in inside diameter, 1 inch in outside diameter, 0.1 inch in wall thickness, and 4 inches tall was then affixed to the surface of the CRFP square where the threaded tip of the screw was protruding using a marine adhesive sealant. The other side of the screw emerging from the CFRP sheet was also sealed using this sealant in order to prevent any leakage

of the salt water test solution. The salt water test solution used in this experiment was a mixture of 3.5 wt% NaCl in water and was poured into the tube after the sealant had fully cured, filling the tube approximately ¾ full. A full cross-sectional sketch of this setup can be found below in *Figure 2*. The samples were separated into 2 groups: long-term samples, which were first tested in April 2017, and short-term samples, which were first tested in September 2017. The designation for the stainless steel and titanium samples were "SS" and "Ti," respectively, while the numbering of the samples determined whether or not each sample was a short-term or a long-term sample: numbers one through three designating long-term samples, while numbers four and greater designated short-term samples.

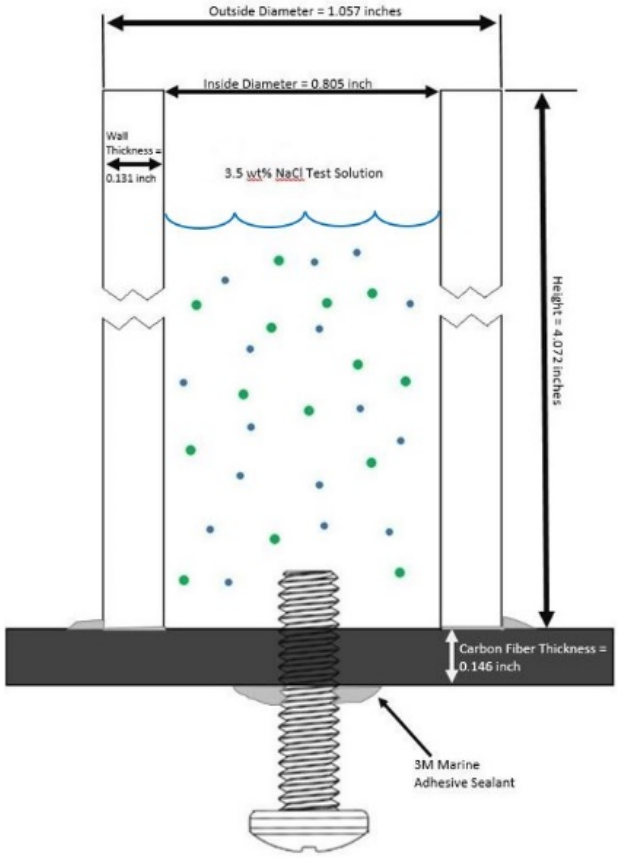

Figure 2: Cross section of the sample setup, indicating the orientation of the screw with the CRFP, the dimensions of the PVC pipe and CFRP panel, and the locations of the marine adhesive sealant. The picture of the machine screw was sourced from the website of a fastener supplier and the jagged cutouts in the side of the tube walls are to signify that the tube height in the figure is not drawn to scale, but is actually much taller than depicted.

ELECTROCHEMICAL TESTING

Potentiodynamic electrochemical impedance spectroscopy (PEIS) measurements were taken using a potentiostat with electrochemical impedance spectroscopy analysis software. This would allow for the measurements of the electrochemical properties of the system without damaging the samples (Park and Yo 2003). The PEIS setup, shown below in *Figure 3*, consisted of the following six sensors indicated in detail in *Figure 4*.

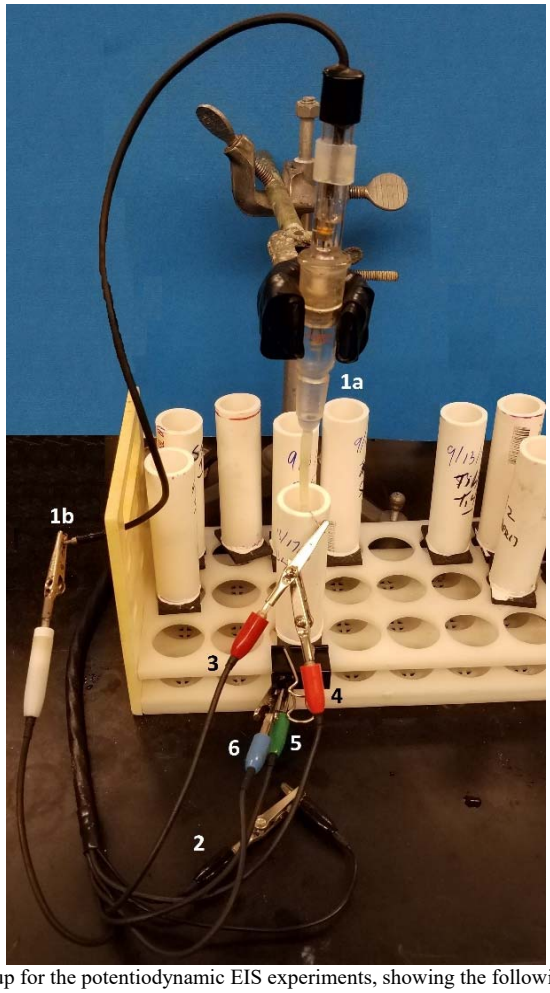

Figure 3: The experimental setup for the potentiodynamic EIS experiments, showing the following: the SCE (1a) attached to the reference electrode (1b); the counter electrode (3) connected to the counter sense electrode (4), with the counter electrode attached to a platinum electrode suspended within the NaCl solution in the tube; the work electrode (5) connected to the work sense electrode (6); and the grounding electrode connected to a grounding wire (2).

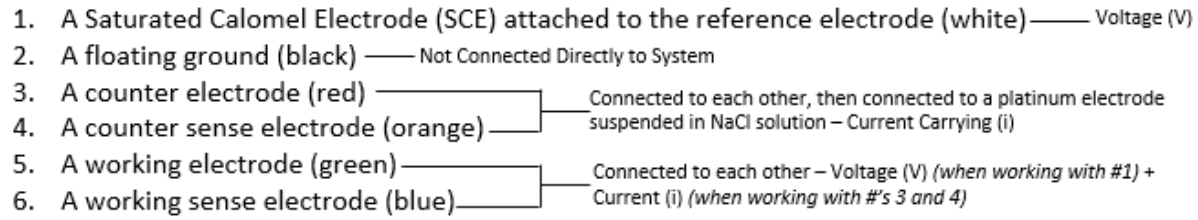

Figure 4: Detail of the six different sensors that are used with the potentiostat and how they relate to one another and to the system as a whole.

The open circuit voltage (OCV) is measured between the SCE and the working electrode, which sets the voltage for the system in units of millivolts (mV). This takes place over a time span of 60 seconds. After those 60 seconds, a sinusoidal voltage of ±10 mV is applied around the OCV value. The resulting current is then measured between the working electrode (5 and 6) and the counter electrode (3 and 4). This current runs in a sinusoidal pattern and the maximum current (i_{max}), along with the maximum of the aforementioned applied voltage (V_{max}) is used to calculate the system impedance (Z) via the following equation (Park and Yo 2003):

$$Z = \frac{V_{max}}{i_{max}}; \qquad (2)$$

The graphical analysis of the two data streams (voltage and current) can also be used to determine the phase angle (ϕ), in which the distance between the peaks of both curves, the V_{max} and the i_{max}, equals the phase angle. Both of these data points can then be used to model the system, in which electrical elements representing the electrochemical system resistance can be determined. This modeling is discussed later in this section.

Once the electrodes were properly connected, as shown in *Figure 3*, different parameters were set within the PEIS software. Some of the parameters included: the initial and final frequencies (Hz), the AC Voltage setting, the DC voltage setting, and the optimization setting. The parameters used in these tests are shown below in *Figure 5*.

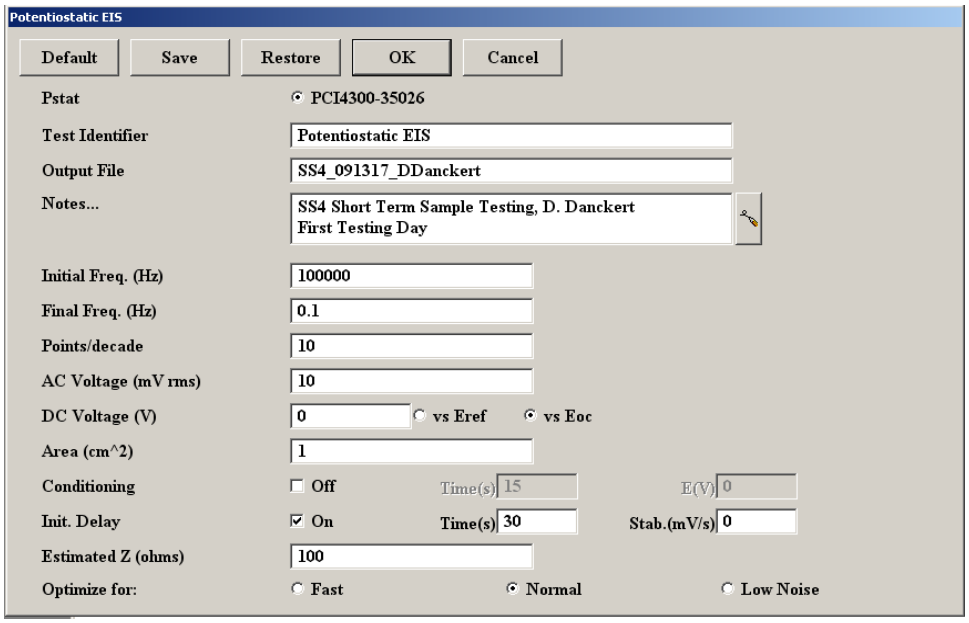

Figure 5: The Software Interface of the Potentiostat, showing the settings that were input for the testing procedure. These include the initial frequency (100 kHz), the final frequency (0.1 Hz), the setting to the DC Voltage to be vs. open circuit voltage (E_{oc}), the output file name, and any pertinent notes for that particular test.

After the experimental setup was completed as stated above, the measurement process was run. This measurement process was run three times per week, on Monday, Wednesday, and Friday, for approximately 70 days, in order to obtain data on the short-term impedance changes of each sample. This short-term data would be used to determine the immediate changes occurring within each sample and to calculate the immediate corrosion rate of each sample. The long-term samples had been tested intermittently between April and September, but were then also tested three times per week, on Monday, Wednesday, and Friday, at the same time as the short-term samples. The purpose of allowing the long-term samples to sit from April to September without regular, periodic testing was to determine whether or not any significant changes in measureable impedance could be observed in the data from those samples after a length of time greater than that the testing period of the short term samples.

PEIS ANALYSIS

The data collected was then analyzed through a proprietary analysis software program in order to determine which passive circuit elements, resistors, and constant phase elements were present in the data. This was performed by running the collected data through different electrochemical circuit element models (Lasia 1999) containing between 2-4 resistors and constant phase elements[1] in parallel. An example of a 3-RC model is shown below in *Figure 6*. By running the collected data through a particular model, a line fit of the data could be achieved with the end-goal being to find a best line fit of the data sets. Based on the best line fit, one could then determine the number of corrosion interfaces present in the system. Additionally, one could use the models to determine the resistance values of each interface as well as the resistance value of the solution, thereby helping to theorize what the different interfaces present are. This data could in turn be used to calculate the corrosion rate at various times throughout the experiment (Lasia 1999).

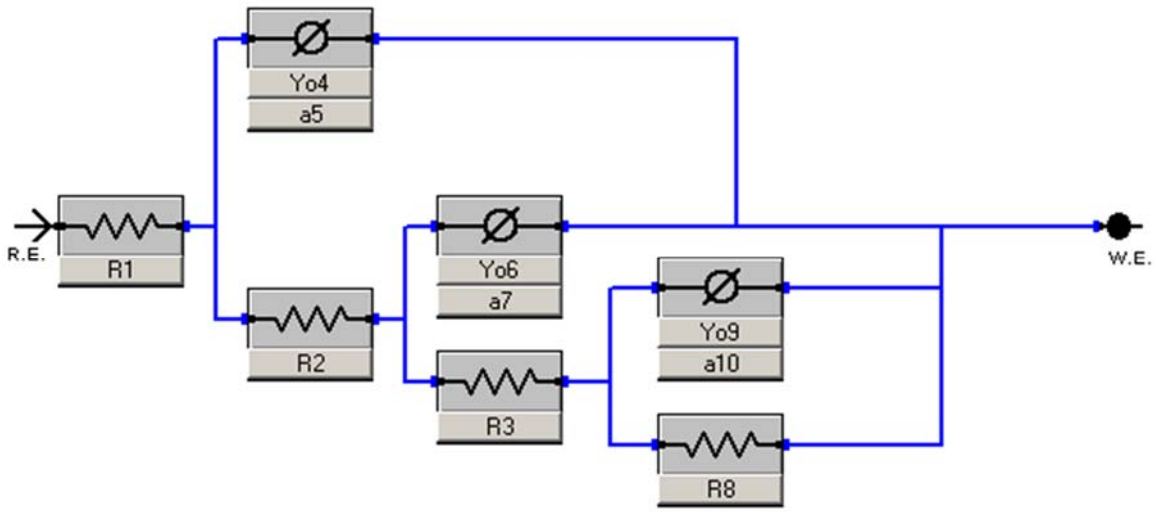

Figure 6: An example of one of the models used to analyze the data within the PEIS software, with this particular model containing 3 Randles Circuits. Pictures of the other models used in the analysis can be found in Appendix A. Each Randles Circuit consists of one resistor and one constant phase element.

[1] A constant phase element is, in its most basic sense, a slightly imperfect capacitor. It allows the model to take into account any imperfections in the capacitance of the system.

SEM EXAMINATION

For the qualitative portion of the experiment, it was required to examine the samples under a scanning electron microscope (SEM) after the data collection portion had been completed. This was accomplished by examining the trend of the open circuit voltage (E_{oc}) values of each sample from the PEIS analysis that were recorded after running for 60 seconds. In the interests to time, only one sample from each set was chosen. In addition, it was decided to choose samples from the long-term sample sets, again in the interest of time as well as the thought that, if any of the samples exhibited mechanical damage due to the corrosion of the metal screws, then the long-term samples would more likely to exhibit this damage than the short-term samples. As such, samples SS2 and Ti2 were selected for the SEM analysis. The machine screws were carefully extracted from the CFRP panels, after which any residual sealant was carefully removed from the screws. The screws were then placed into the SEM along with the CFRP panels for examination. In order to be able to ascertain the location of the screw that had been inserts into the CFRP panel, copper tape was used to mark the screw, as shown below in *Figures 7* and *8*. Copper tape was used because it would not degrade within the vacuum chamber of the SEM and would not adversely affect the screws. Then, using the SEM, the CFRP panels were each examined to determine whether or not the corrosion product from the inserted screw has caused any mechanical damage to the CFRP. The screws were also examined to determine which corrosion processes, if any, had affected each screw. This observation formed the

basis of the qualitative portion of the experiment and dictated how the quantitative data could be used.

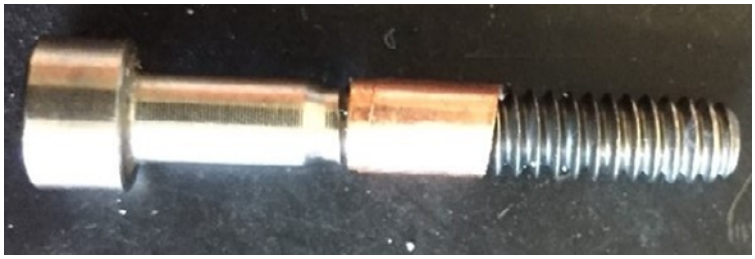

Figure 7: The machine screw from the Ti2 sample after being extracted from the CFRP panel. The copper tape was placed in such a way to allow for the determination of the parting line where the titanium machine screw was inserted into the CFRP panel.

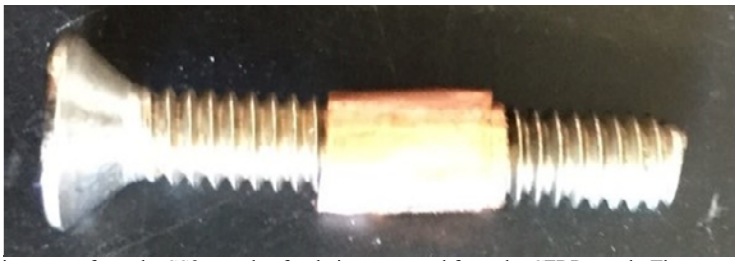

Figure 8: The machine screw from the SS2 sample after being extracted from the CFRP panel. The copper tape was placed in such a way to allow for the determination of the parting line where the stainless steel machine screw was inserted into the CFRP panel.

During the SEM analysis, if any interesting features or deposits were found on the surfaces of either the screws or the CFRP panels, they could be analyzed for chemical composition with energy-dispersive X-ray spectroscopy (EDS) via the EDS spectrometer mounted to the SEM. The EDS would allow for elemental analysis or chemical characterization of a selected point on the surface of the sample via reading the emission x-rays from the selected point. In order to stimulate the emission of those x-rays, a high-energy beam in the form of charged particles, such as electrons, would be shot at the selected point. This process is known as particle-induced x-ray emission, or PIXE (Shindo and Oikawa 2002). This would excite the individual atoms within the selected point to the point where the atoms at the selected point are induced to emit x-rays. The x-rays emitted by the different elements are unique to that element, and can therefore be read by the EDS (Shindo and Oikawa 2002). While the

EDS would not be able to determine the molecules present at a selected point, being able to ascertain the elements present would allow for a determination if any corrosion product, or other foreign substance, was present on the CFRP or on the individual screws. The EDS added a qualitative and a quantitative portion to this study.

CHAPTER 4

RESULTS AND DISCUSSION

Due to the time constraints present in this study, only one sample from each set could be chosen for analysis. Based on this, the long-term samples were focused on due to the theory that, if any corrosion-related damage to the CFRP panel would be seen, then it would more likely been seen on the long-term samples due to the longer residence time in salt water experienced by the samples. As such, SS2 and Ti2 were selected for the analysis portion of this study as they were exposed for 7 months.

SEM ANALYSIS RESULTS – TITANIUM SAMPLE

The first sample set that was examined under the SEM was one of the titanium samples, specifically the long-term sample Ti2. Once the sample was removed from the CFRP panel and any excess sealant was carefully removed, the surface of the screw was visually inspected. It was noted that a slight black discoloration was evident on the surface of the screw, as shown below in *Figure 9*, for which the cause was not immediately evidence. The CFRP was also visually inspected to check for any evident signs of damage. Nothing immediately apparent was noticed.

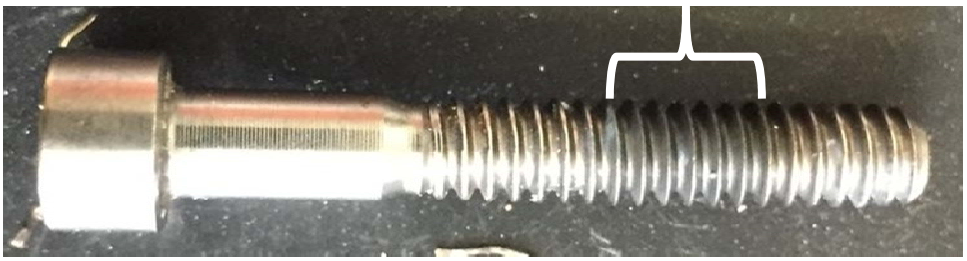

Figure 9: The titanium screw from sample Ti2 after it was extracted from the CFRP panel and had any remaining sealant carefully removed. Note the apparent lack of any corrosion-related damage as well as the presence of a slight blackened area, indicated by the bracket. The blackened area is where the screw was in direct contact with the CFRP. Picture is courtesy of Jordan A. Ortiz.

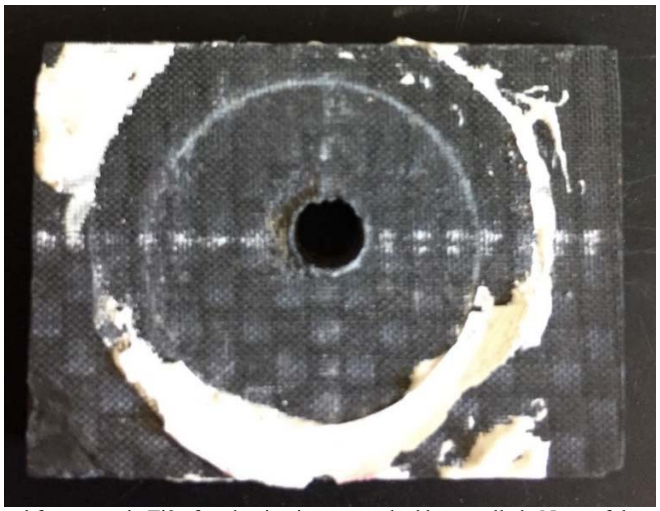

Figure 10: The CFRP panel from sample Ti2 after the titanium screw had been pulled. None of the sealant was removed from the surface as this might have damaged the surface of the CFRP. Note the light white circles around the threaded hole, which potentially are deposits of NaCl from the salt water. Picture is courtesy of Jordan A. Ortiz.

After the visual inspection, both the screw and the CFRP panel were examined in the SEM as described in the methodology section. Visual inspection of the sample showed no degradation of the threaded region of the screw, as seen below in *Figure 11*.

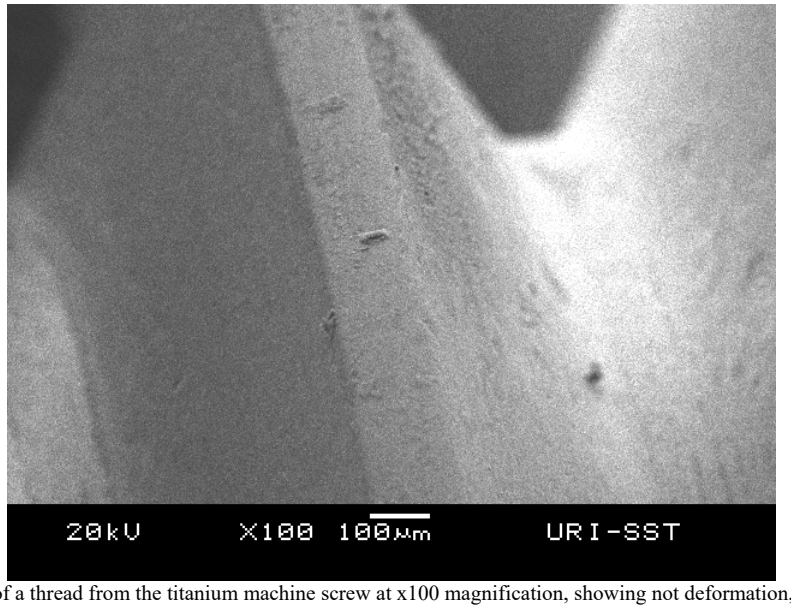

Figure 11: Image of a thread from the titanium machine screw at x100 magnification, showing not deformation, and as a result no evidence of a corrosion process. The entire thread region that was threaded of the screw that was in the CFRP panel was examined and found to be in the same condition.

Additionally, using EDS, the surface of the threads was examined to determine if the presence of any apparent corrosion product could be determined. In the EDS

results, the only prominent peaks that the system could identify were titanium and aluminum. Given that aluminum is a common alloying element for titanium, it was determined that this was the most likely source of the aluminum. No other significant element presences were found, indicating little-to-no corrosion product on the surface of the screw threads that were within the CFRP panel. The EDS results of the titanium screw are shown below in *Figure 12*.

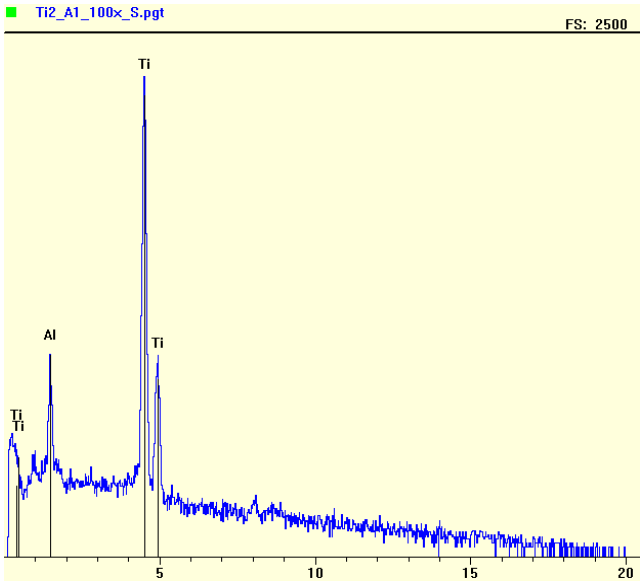

Figure 12: The results of the EDS analysis performed on the Ti screw sample within the SEM chamber, showing prominent peaks for titanium and aluminum. Since aluminum is a common alloying element used with titanium, it was determined that the aluminum being detected was from the machine screw.

After the titanium screw had been examined, the CFRP panel into which the titanium screw had been affixed was also examined. The first observation made was that there was no apparent mechanical damage to the CFRP around the threaded hole. There was a dulled area around the hole that appeared to potentially be damage, but upon closer examination, the root cause of this deformation appeared more likely to be a side-effect of the drilling and tapping process that was performed during sample setup. Additionally, some carbon fibers from the CFRP structure appeared to have been bare. It could be theorized that is the epoxy originally covering those fibers had

somehow been removed, but whether this was a function of the sample preparation process or the testing process could not be determined.

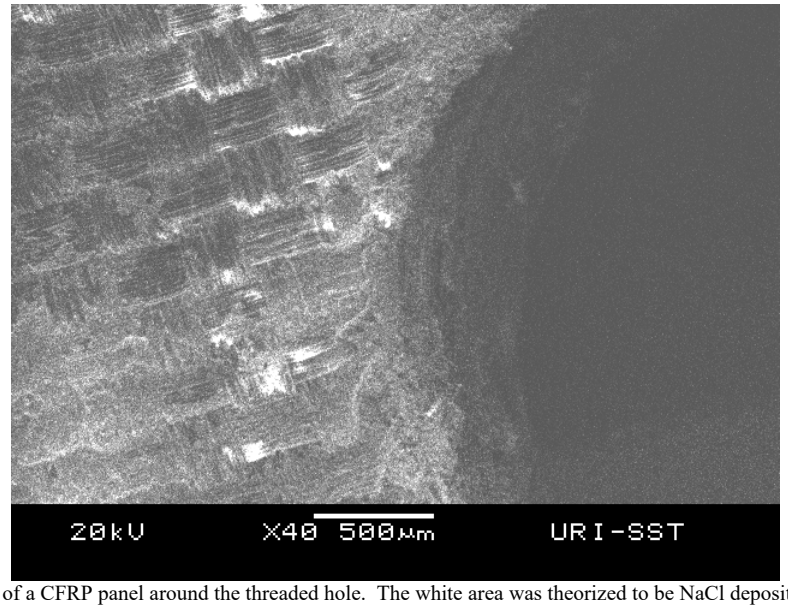

Figure 13: Image of a CFRP panel around the threaded hole. The white area was theorized to be NaCl deposits. The roughened area around the threaded hole was most likely caused by the sample preparation process. Additionally, there appeared to be some bare carbon fibers on the surface of the CFRP panel, but the root cause of this could not be determined.

As mentioned at the beginning of this section, light, white rings could be seen on the surface of the CFRP panel where the CFRP had been directly exposed to the salt water solution. It was theorized that those white rings were deposits of NaCl. To validate this theory, those white rings were subjected to the EDS analysis. The resulting graph, shown below in *Figure 14*, showed the most prominent peaks being sodium and chlorine, indicating that there was a high likelihood that the white deposits were indeed NaCl deposits. Some additional peaks showed the presence of iron and silicon. It is possible that these elements were present within the structure of the CFRP, but since the exact make-up of the CFRP is unknown due to the makeup of the CFRP used being proprietary, this hypothesis cannot be confirmed or denied.

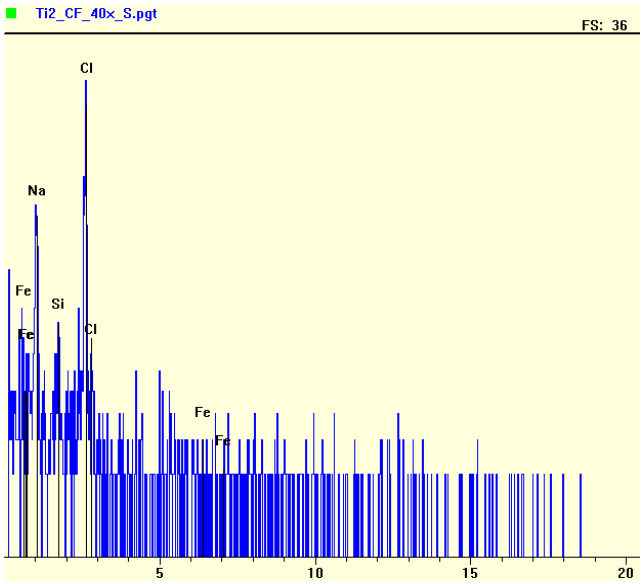

Figure 14: The results of the EDS analysis performed on the Ti2 CFRP panel same within the SEM chamber, showing prominent peaks for sodium and chlorine, which confirms the presence of NaCl deposits on the surface of the CFRP panel. Prominent peaks are also shown for iron and silicon. It is possible that these elements were already present in the structure of the CFRP, but, due to the proprietary nature of the CFRP's make-up, this cannot be confirmed.

PEIS EXPERIMENTAL RESULTS – TITANIUM SAMPLE

After visually analyzing the Ti2 sample under the SEM, the PEIS data was analyzed in an effort to be able to better quantify the Ti2 system with numerical data in the form of a measured system impedance. Since sample Ti2 was a long-term sample, only three short-term data points were available, which did not allow for a good short-term corrosion trend to be established with this sample. Long-term corrosion characteristics of the system could however be established and, based on the data graphically displayed in *Figure 15*, the Ti2 system remained fairly stable, which would substantiate titanium propensity for forming an extremely stable oxide layer that hinders the corrosion process after formation (Rebak 2013).

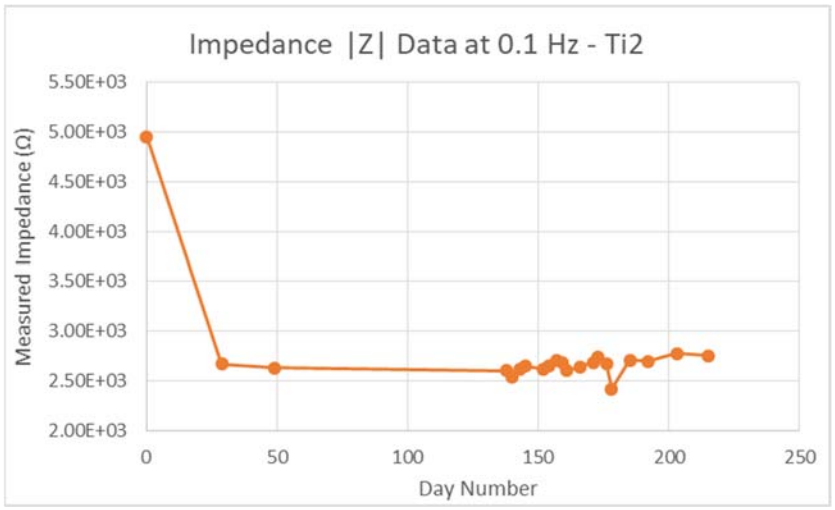

Figure 15: The impedance data at 0.1 Hz frequency for the Ti2 sample. The PEIS data encompassed a frequency range of 0.1 Hz - 0.1 MHz, but the 0.1 Hz data points were chosen for analysis due to the fact that the electrical current measured by the PEIS system at the lower frequencies is more likely to follow the rather of the resistor with the Randles Circuit rather than the path of the constant phase element.

From the data graphically displayed in *Figure 15*, dates were selected to subject to the modeling process within the PEIS software. The modeling process would allow for the determination of the number of interfaces suggested to simulate the electrochemical behavior of the titanium screw-CFRP composite system. For the modeling process, the first four dates were selected due to the first three representing the cumulative short-term data available for Ti2 and the fourth representing the beginning of the weekly testing regiment described in the methodology section, which in this case was 13 September 2017. Given the relative stability of the impedance values exhibited by the Ti2 samples, it was determined that only two additional dates would need to be selected for the modeling. As such, the final date of testing was selected as well as an additional date in between the end date and the 13 September 2017 date. All dates selected for the modeling, along with their residence day number and the impedance value at 0.1 Hz, are listed below in *Table 1*.

Date	Day #	Impedance (Ω)
4/28/2017	0	4.95E+03
5/27/2017	29	2.67E+03
6/16/2017	49	2.63E+03
9/13/2017	138	2.60E+03
9/15/2017	140	2.53E+03
9/18/2017	143	2.61E+03
9/20/2017	145	2.65E+03
9/27/2017	152	2.62E+03
9/29/2017	154	2.65E+03
10/2/2017	157	2.71E+03
10/4/2017	159	2.69E+03
10/6/2017	161	2.60E+03
10/11/2017	166	2.64E+03
10/16/2017	171	2.69E+03
10/18/2017	173	2.74E+03
10/21/2017	176	2.67E+03
10/23/2017	178	2.42E+03
10/30/2017	185	2.71E+03
11/6/2017	192	2.70E+03
11/17/2017	203	2.78E+03
11/29/2017	215	2.75E+03

Table 1: The impedance values of the Ti2 system at 0.1 Hz, along with the date tested and the applicable residency day of each particular data point. The values in **GREEN** indicate the dates that were subjected to the PEIS data modeling.

With the dates selected, as shown in *Table 1*, the modeling process was started with the data sets from each of the selected dates being run through a 2RC, a 3RC, and a 4RC model. After each model was run, a fitment line was superimposed over the data points collected by the PEIS system. The PEIS system then calculated a goodness of fit value based on how close the superimposed line fit to the data points, with smaller values signifying a better fit to the data. An example of the graph fits from the PEIS software is seen below in *Figure 16*, along with the goodness of fit values for all dates that were subjected to the modeling process.

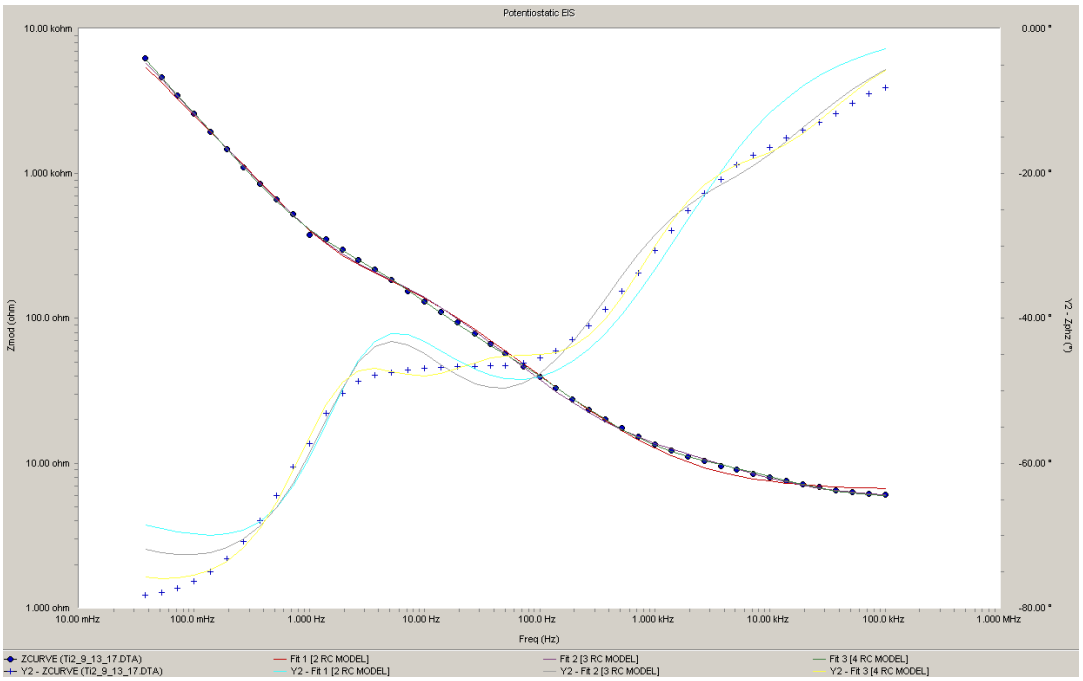

Figure 16: Modeling results of Ti2 data from 9/13/2017 after the 2RC, 3RC, and 4RC models had all been run. Note the varying degrees of fit for each model. Additional graphs can be found in Appendix B.

Goodness of Fit – Ti2	2 RC	3 RC	4 RC
4/28/2017	9.51E-03	**2.35E-04**	2.42E-04
5/27/2017	9.18E-03	2.51E-03	**2.50E-03**
6/16/2017	7.10E-03	7.10E-03	**2.58E-03**
9/13/2017	9.00E-03	3.01E-03	**7.08E-04**
10/21/2017	5.51E-03	6.25E-03	**2.23E-04**
11/29/2017	7.92E-03	2.39E-03	**1.28E-03**

Table 2: Goodness of fit values generated by the PEIS software for the selected Ti2 data sets to analyze how close the generated line for each model came to fitting the actual data. The closer the value came to "0", the better the fit.

After analyzing the fitment data listed above in *Table 2*, it was determined that, overall, the best model fit came from the 4RC model, which would indicate that four interfaces were present within the system as time progressed. The first sample date, 28 April 2017, indicated that there were three interfaces at play. It was theorized that the three interfaces present at the very beginning of the testing process:

1. Titanium machine screw to the NaCl solution
2. CFRP panel surface to the NaCl solution
3. Titanium machine screw to the CFRP panel

As the testing progressed, the system appeared to shift from a three interface setup to a four interface setup, based on the goodness of fit values calculated by the PEIS software, as shown in *Table 2*. Based on this data, the fourth interface was determined to be the metal oxide layer to the NaCl solution.

SEM ANALYSIS RESULTS – STAINLESS STEEL SAMPLE

The second sample set that was examined under the SEM was one of the stainless steel samples, specifically the long-term sample SS2. Once the sample was removed from the CFRP panel and any excess sealant was carefully removed, the surface of the screw was visually inspected. It was noted that a slight discoloration was evident on the surface of the screw, as shown below in *Figure 17*. This discolored area had been in direct contact with the CFRP panel during the experimental portion of this study. Within this discolored area, a roughened area on a thread was also noticed, as depicted in *Figure 17*. The CFRP was also visually inspected to check for any evident signs of damage. Some reddish-brown discoloration was evident around the threaded hole, which could potentially have been a product of corrosion of the stainless steel screw. This can be seen in *Figure 18*. Additionally, the surface of the CFRP panel also exhibited significantly higher amount of white deposits, which were potentially NaCl that had dried on the surface of the CFRP panel.

Figure 17: The stainless screw from sample SS2 after it was extracted from the CFRP panel and any remaining sealant was carefully removed. Note the slight blackened area, indicated by the bracket. The blackened area is where the screw was in direct contact with the CFRP. Additionally, there appears to be a roughened area on one of the threads, as indicated by the red circle. This roughened area may be a sign of corrosion damage. Picture is courtesy of Jordan A. Ortiz.

Figure 18: The CFRP panel from sample SS2 after the stainless steel screw had been pulled. None of the sealant was removed from the surface as this might have damaged the surface of the CFRP. Note the significant white deposits present on the surface where the CFRP was in contact with the salt water. These white deposits are most likely solidified NaCl from the salt water. Additionally, note the reddish-brown coloring around the edges of the threaded hole, which could potentially indicate a corrosion product from the stainless steel screw. Picture is courtesy of Jordan A. Ortiz.

After the initial visual inspection, both the screw and the CFRP panel were examined in an SEM as described in the methodology section. The images seen on the SEM were markedly different when compared to those observed with the titanium screw. As shown below in *Figure 19*, a portion of the screw thread peak appeared to have been eaten away by the corrosion product over the course of the 70-day experimental period. Upon closer examination, there appeared to be small nodules along the surface on the affected surface. EDS was conducted on these nodules in an

attempt to determine their chemical composition. Based on the EDS analysis shown in *Figure 21*, the predominant elemental signatures present were from iron and chlorine, indicate the potential presence of an iron chloride compound. Other elements suggested to be present were nickel and chromium, which would be expected as these elements were directly in the stainless steel screw.

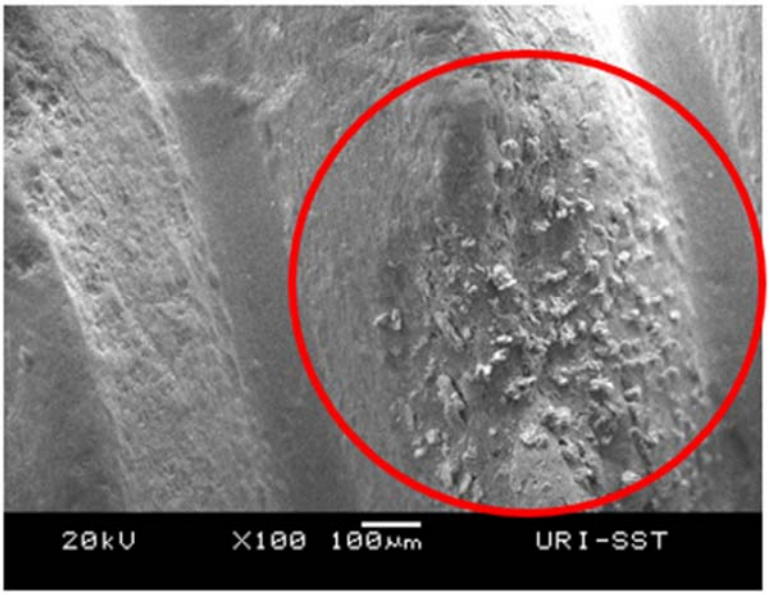

Figure 19: Image of a thread from the stainless steel machine screw at x100 magnification, showing signs of significant crevice corrosion (area in question signified by the **RED** circle). The particular thread pictured above appears to have been eaten away, leaving behind small nodules.

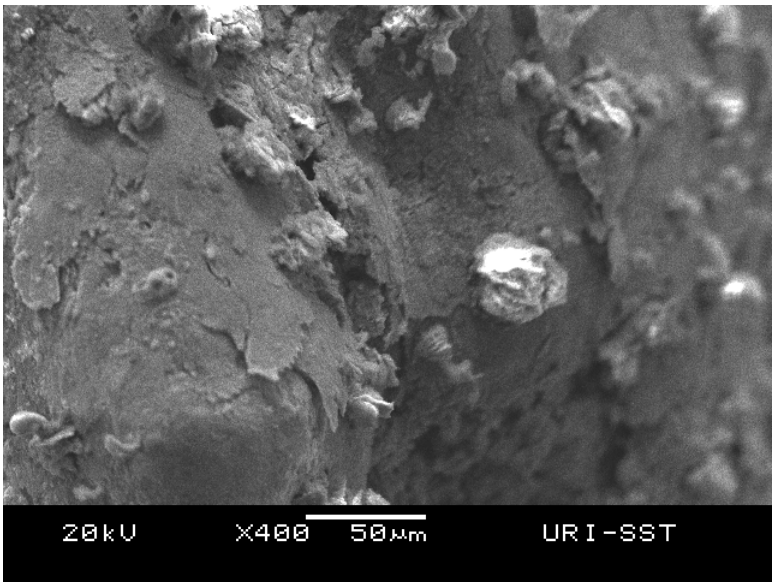

Figure 20: A close-up image of the nodules mentioned in *Figure 19*. These nodules were subjected to a chemical analysis with the SEM's EDS.

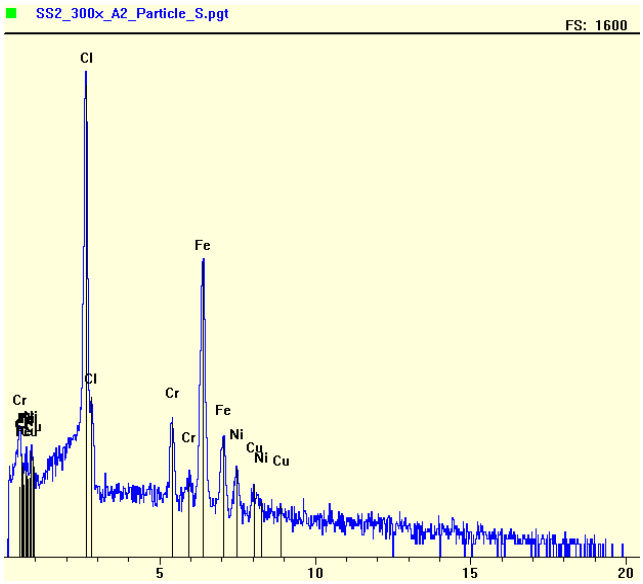

Figure 21: The results of the EDS analysis performed on the nodule pictured in *Figure 19*. Significant portions of iron and chlorine were present on the nodule, potentially signifying the presence of an iron chloride compound. The chromium and nickel found in the EDS scan are most likely from the stainless steel screw, since both elements are alloying elements in stainless steel.

After examining the portion of that had been direct contact with the CFRP, the section of the screw that had been directly exposed to the salt water solution was examined next. The majority of this portion of the screw was still intact, not exhibiting any of the severe corrosion that was observed on the portion of the screw that had been in direct contact with the CFRP panel. There was however one portion of the screw that appeared to exhibit the beginnings of pitting corrosion, shown below in *Figure 22*. This apparent occurrence of pitting corrosion was found in a valley between 2 threads. Pitting corrosion was not readily observed in other areas of this screw.

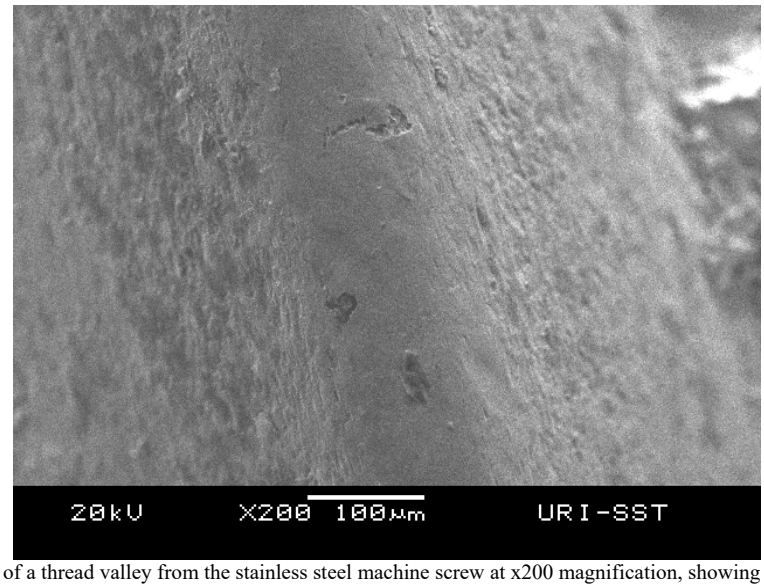

Figure 22: Image of a thread valley from the stainless steel machine screw at x200 magnification, showing signs of significant pitting corrosion. This area of the screw was not in direct contact with the CFRP panel.

While no additional instances of pitting or crevice corrosion was found on the screw, some "nodules" were found near the location of the pits shown in *Figure 23*. This nodule appeared to be different from the nodules found in the instance of crevice corrosion shown in *Figures 19-20*, specifically in the fact that these nodules were cubic while the others had been moderately round. EDS analysis indicated that these square nodules were NaCl deposits that had solidified on the surface of the screw.

Figure 23: An image of another nodule found on the stainless steel screw in an area that was not in direct contact with the screw. Further analysis via the EDS confirmed this to be an NaCl crystal, not necessarily a byproduct of the corrosion process, specifically the pitting corrosion seen in *Figure 22*.

After analysis of the screw was completed, the matching CFRP panel was analyzed. The first observation made on this panel was the stark difference it represented when compared to the CFRP from sample Ti2. Unlike Ti2, which had exhibited no mechanical damage, the CFRP panel associated with sample SS2 exhibited several areas with varying degrees of delamination, as shown in below in *Figures 24-27*.

The first area observed, shown below in *Figure 24*, was dubbed the "southern" end of the threaded hole, showed some white build-up that was most likely NaCl deposited on the surface. The more interesting feature was the apparent shards of CFRP that were breaking off from the surface of the panel. It was considered possible that these shards could have been initially formed during the sample preparation process, but then some areas of delamination were noticed in close proximity to these shards. This meant that these shards could have been the result of delamination induced by the corrosion process of the stainless steel screw.

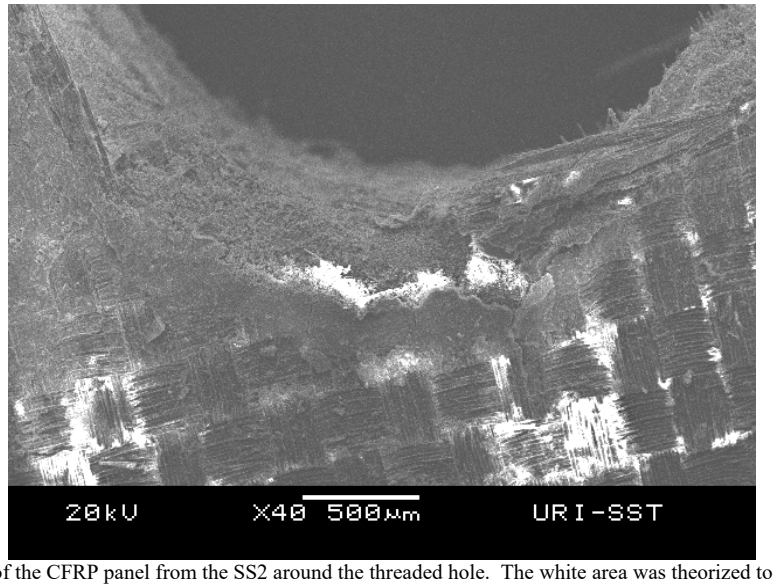

Figure 24: Image of the CFRP panel from the SS2 around the threaded hole. The white area was theorized to be NaCl deposits. The roughened area around the threaded hole was appeared to show shards to CFRP breaking away from the main portion of the panel. While this could have been caused during the sample preparation process, a small area of delamination was noticed near the shards, which would most likely not have been caused by the sample preparation process. As such, these shards could have come from either the sample preparation process or could have been a byproduct of the corrosion of the screw.

To further analyze the surface around the threaded hole, other areas needed to be examined. *Figure 25* below shows the second area that was dubbed the "northern" end of the hole. The particular area, while not exhibiting the "shards" seen in *Figure 24*, showed clearer signs of delamination around the edges of the threaded hole. While not a definitive indication that the corrosion of the stainless steel screw was causing damage to the structure of the CFRP, the delamination at this point could not have been caused by the sample preparation process and, as such, was most likely caused by the corrosion process.

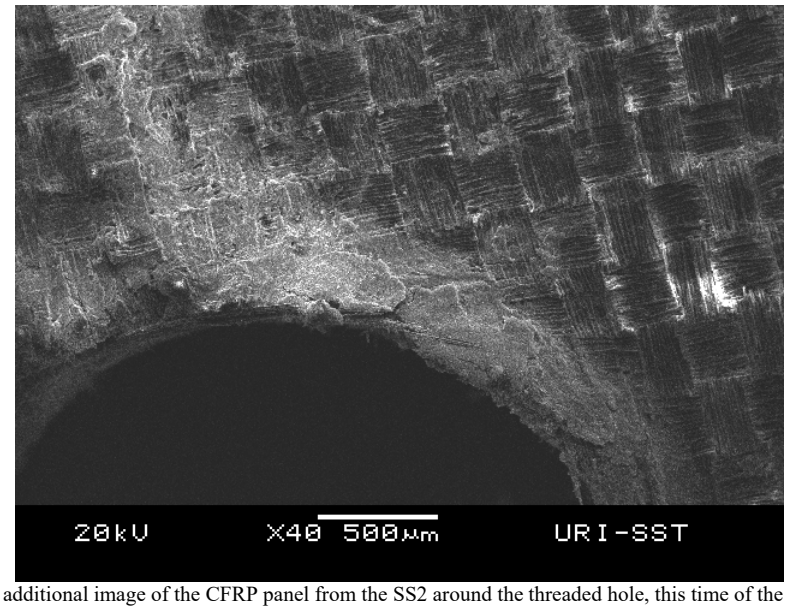

Figure 25: An additional image of the CFRP panel from the SS2 around the threaded hole, this time of the "northern" side. Again, the white area was theorized to be NaCl deposits. The roughened area around the threaded hole was appeared to be delamination of the CFRP panel, which most likely did not occur during the sample preparation process. It is possible that this delamination was caused by the corrosion process of the screw.

After analyzing the northern side of the threaded hole, the CFRP panel was shifted to investigate the "western" side, shown below in *Figures 26 and 27*. Out of all the areas investigated, this particular section appeared to give the clearest indication of some sort of mechanical damage having occurred. While it was remotely possible that this could have been caused by the sample preparation process, given that the both CFRP panels examined under the SEM did not exhibit this level of damage, it

is highly unlikely that this was caused by the drilling and tapping of the CFRP panel. Additionally, this sample exhibited a significant build-up of white deposit around the affected area.

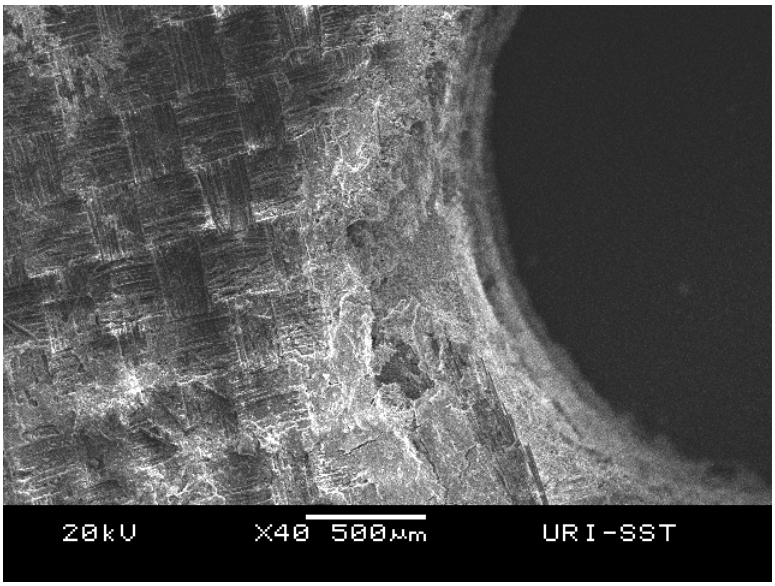

Figure 26: A third image of the CFRP panel from the SS2 around the threaded hole, this time of the "western" edge. As before, the white area was theorized to be NaCl deposits. The delamination observed in this area was noticed to be the most severe when compared to the other area around the threaded hole. The delamination is so severe that it appears that layers of the CFRP have flaked away.

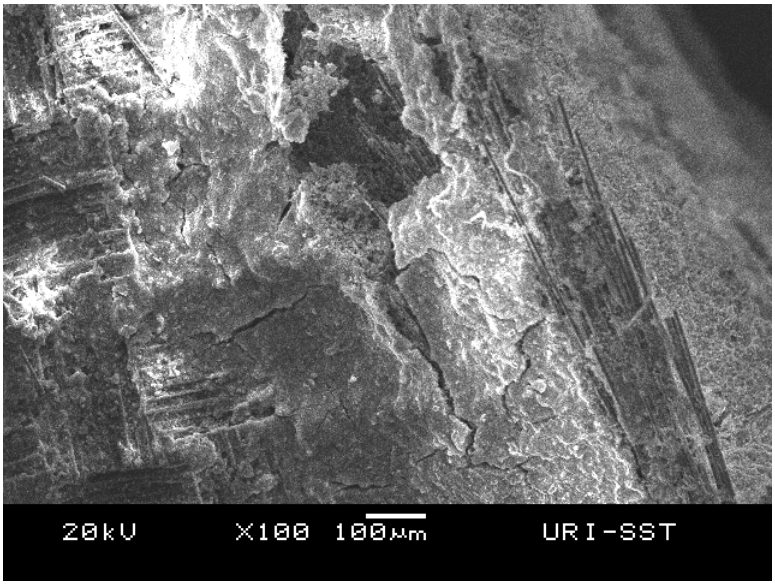

Figure 27: A close-up of *Figure 26*, showing the severity of the delamination. This image also appears to show strands of carbon fiber that were freed from the CFRP matrix.

To confirm that the white deposits were in-fact crystallized NaCl, a selected area was subjected to EDS analysis. The results of this, along with the specific region

that was analyzed, is shown below in *Figure 28*. The EDS test results overwhelming confirmed the presence of NaCl, along with a trace amount of iron. The most likely source of the iron within the scan was the corrosion of the stainless steel screw.

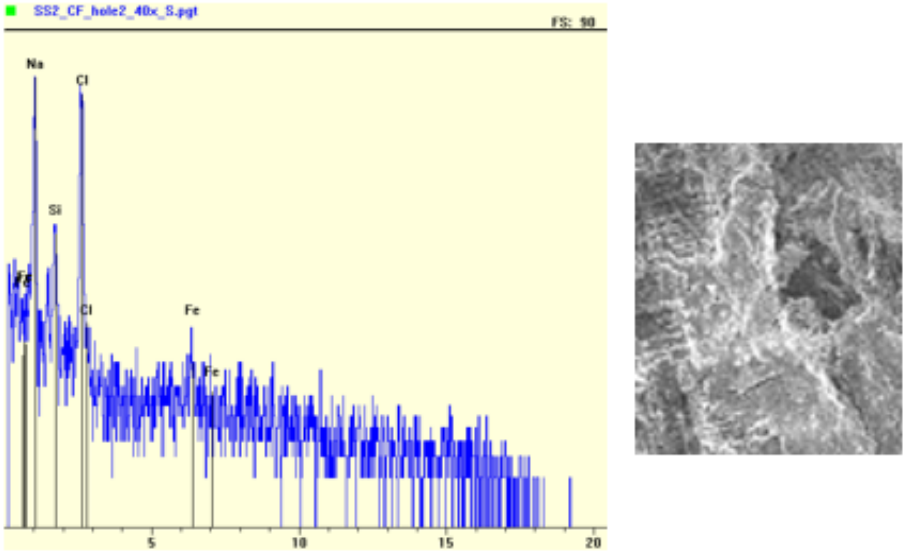

Figure 28: An EDS analysis of the white deposits shown in *Figure 26*, along with an image of the specific section that was tested. This indicates that the deposits are mainly solidified NaCl with some iron present. The small presence of iron detected in the scan is most likely a byproduct of the corrosion of the stainless steel screw.

Having confirmed the presence of NaCl along the surface of the CFRP panel, focus was shifted to another section of *Figure 26* that appeared to show an area where the CFRP had delaminated to an extent where it had flaked away and exposed a sublayer of the CFRP matrix. While it did appear that this area must indicate that the CFRP was subjected to some sort of deformation, potentially from the corrosion product of the stainless steel screw, it could not be confirmed or denied solely based on a visual observation. As such, this area was subjected to EDS analysis as well to determine which chemical elements were present on that surface. The results of this EDS test, along with a view of the area tested, is shown in *Figure 29*. The test results clearly indicated a high amount of iron present, which could only have come from the stainless steel screw. Given the previously-discussed state of the stainless screw, the

iron deposits most likely came during the corrosion process experienced by the stainless steel screw. As such, this visual analysis along with the EDS results seem to lend credence to this study's hypothesis.

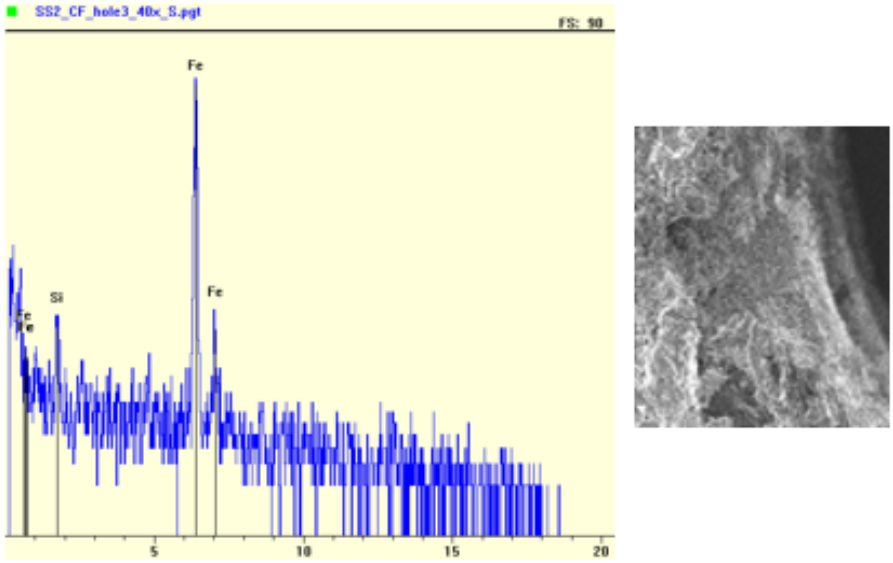

Figure 29: An EDS analysis of the area shown to the right which represents an area around the threaded hole that is below the surface level of the CFRP panel. This area was exposed due to the delamination and flaking away of the layers above and it was theorized that this delamination was caused by the corrosion of the stainless steel screw. The EDS results showed high amounts of iron, which seems to indicate a significant presence of an iron-based corrosion product. This find could lend credence to the hypothesis of this thesis.

In order to get a better view of the threads within the CFRP panel so as to gather more evidence to substantiate this study's hypothesis, the CFRP panel from the SS2 sample was carefully cut in half to expose the threads for better analysis on the SEM. This operation was not performed on the CFRP panel for the Ti2 sample because, unlike the SS2 sample, no damage to the CFRP had been observed.

The first visual analysis, shown in *Figure 30*, shows the inside of the threads within the CFRP panel for the SS2 sample. Unlike with *Figures 24-27*, this image did not display any concrete evidence to support this study's hypothesis. While there did appear to be some loose strands of carbon fiber within the threads, it could not be confirmed whether or not this could have been caused by the corrosion process, as

these strands could also have been dislodged during the sample preparation process. On item of note from this figure was the presence of white deposits on the surface of the threads. These deposits could either have been solidified NaCl, as had been seen on the topside surface of the CFRP panel, or it could have been some sort of product from the corrosion process, as a whitish product of the corrosion process had been observed on the surface of the stainless steel screw, as seen in *Figure 30*. An EDS analysis would be required to determine the exact chemical composition.

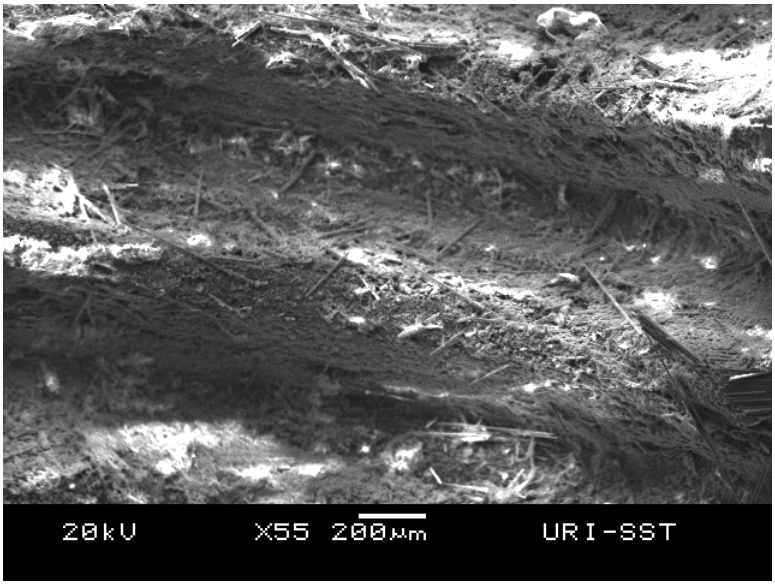

Figure 30: A view from within the threads of the CFRP panel from the SS2 sample. Unlike what was observed in *Figures 24-27*, no mechanical damage was readily apparent that could have been definitely caused by the corrosion of the stainless steel screw. There do appear to be some strands of carbon fiber in this image that would have been loosen by the corrosion process, but these strands could also have been loosened by the sample preparation process. There also appear to be white deposits at several points in this image, which could either be NaCl deposits or a product of the corrosion process.

The second analysis, shown below in *Figure 31*, displays another vantage point of the threads within the CFRP panel. As with *Figure 30*, this image also showed the loose strands of carbon fiber, but again there were no clear signs of mechanical damage that could be definitely traced back to the corrosion process of the stainless steel screw. This image also displayed white deposits on the surface of the threads, as was also seen in *Figure 30*.

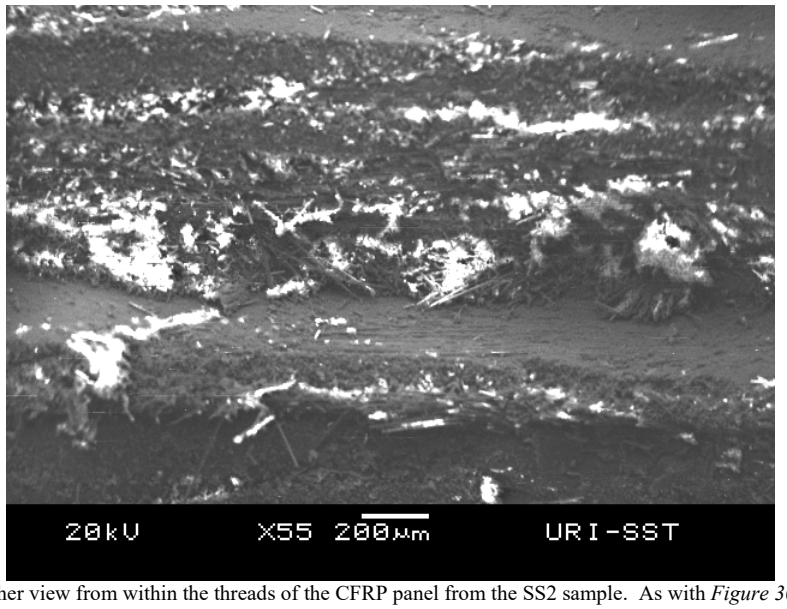

Figure 31: Another view from within the threads of the CFRP panel from the SS2 sample. As with *Figure 30*, no mechanical damage was readily apparent that could have been definitely caused by the corrosion of the stainless steel screw. There also appear to be some strands of carbon fiber in this image, but it could not be confidently ascertained what the source of these threads was. As before, there also appear to be white deposits at several points in this image, which could either be NaCl deposits or a product of the corrosion process. EDS analysis would be required to determine the composition of these deposits.

In order to determine exactly what the chemical composition of the white deposits seen in *Figures 30* and *31* was, the CFRP sample was subjected to an EDS analysis. The results are shown below in *Figures 32A-D*. *Figures 32A* shows the three different locations tested, two points one and two being white deposits and point three being an area without the white deposit. Based on the EDS analysis results from points one and two (*Figures 32B* and *32C*), it was abundantly clear that the white deposits were not solidified NaCl. Instead, based on the presence of high amounts of alloying elements typically found in stainless steel, these white deposits were determined to be a product of the corrosion process of the stainless steel screw, although it could not be definitively determined what that corrosion product was. Point three, while showing a clear spike in the carbon value, still exhibited a significant presence in iron, chromium, and nickel on the surface of the CFRP.

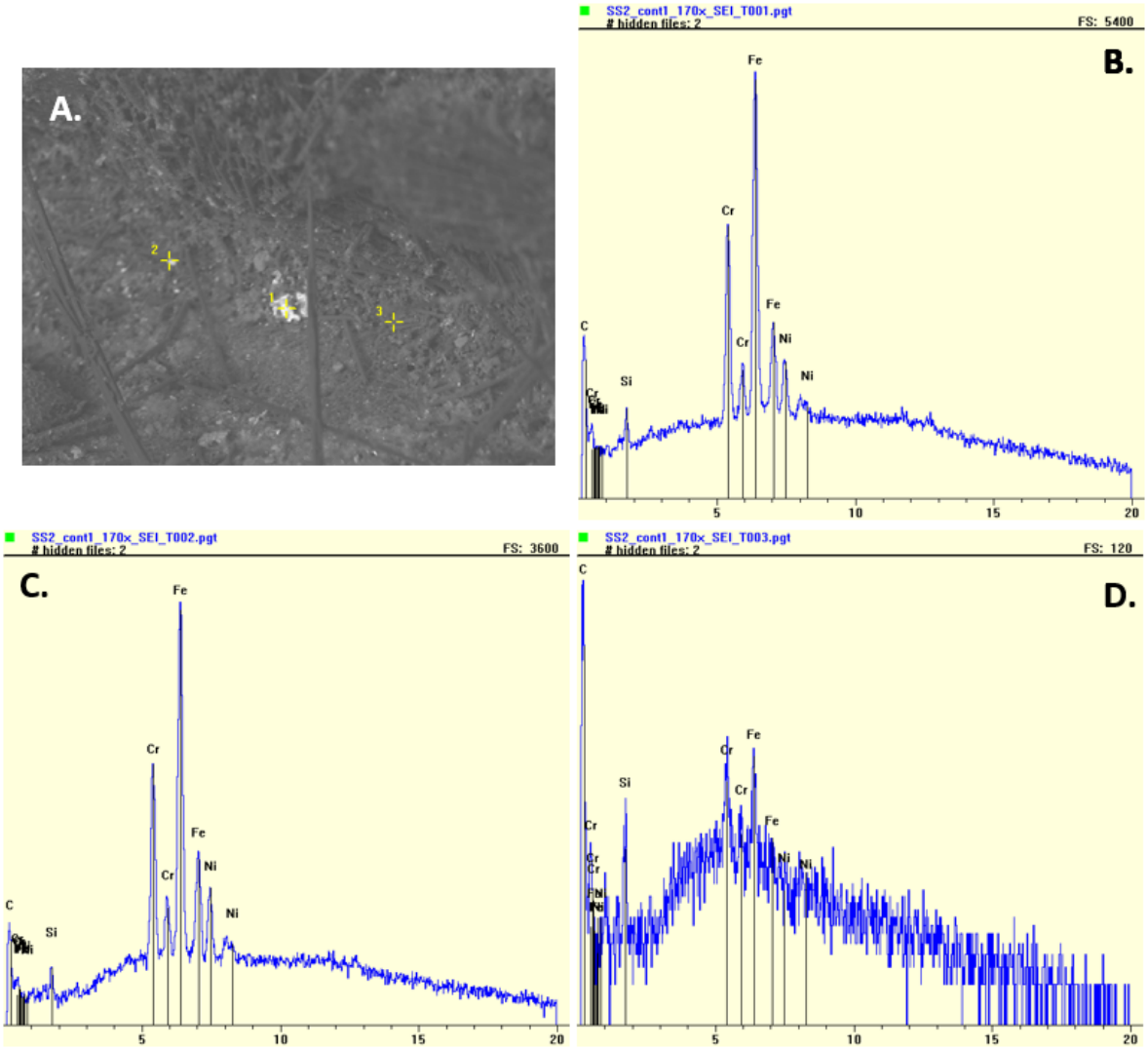

Figure 32A-D: EDS analysis results for the threads, with a main focus on the white deposits found within the threads. *Figure 32A* shows the three positions that was analyzed via EDS. The results for point one (*Figure 32B*) and point two (*Figure 32C*) clearly show that the white deposits were not solidified NaCl, but rather products of the stainless steel corrosion process. The results for point three (*Figure 32D*), which was taken in an area without a white deposit, showed a clear and expected spike in the presence of carbon. Point three also exhibited a significant presence of Fe, Cr, and Ni, all alloying elements in stainless steel.

PEIS EXPERIMENTAL RESULTS – STAINLESS STEEL SAMPLE

After visually analyzing the SS2 sample under the SEM, the PEIS data was analyzed in an effort to be able to better quantify the SS2 system with numerical data in the form of a measured system impedance. Since sample SS2 was also a long-term sample, like the Ti2 previously discussed, only three short-term data points were available, which did not allow for a good short-term corrosion trend to be established

with this sample. Long-term corrosion characteristics of the system could however be established and, based on the data graphically displayed in *Figure 33*, the SS2 system appeared to have greater fluctuation in measured impedance values than the Ti2 system. As such, more data than was needed for the Ti2 system would be required in order to create an applicable model for the system.

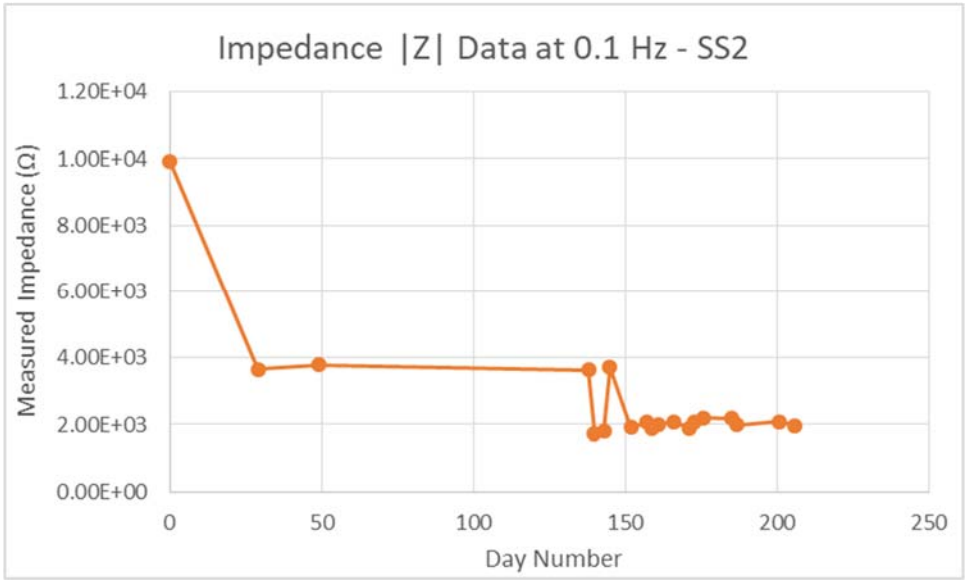

Figure 33: The impedance data at 0.1 Hz frequency for the SS2 sample. The PEIS data encompassed a frequency range of 0.1 Hz - 0.1 MHz, but the 0.1 Hz data points were chosen for analysis due to the fact that the electrical current measured by the PEIS system at the lower frequencies is more likely to follow the rather of the resistor with the Randles Circuit rather than the path of the constant phase element.

From the data graphically shown above in *Figure 33*, dates were selected to be subjected to the modeling process within the PEIS software. The modeling process would allow for the determination of the number of interfaces being detected by the PEIS software based on the data collected. For the modeling process, the first four dates were selected due to the first three dates representing the cumulative short-term data available for Ti2 and the fourth date representing the beginning of the weekly testing regiment described in the Methodology section, which in this case was 13 September 2017. As stated previously, given the fluctuation of the impedance values observed in *Figure 33*, more sample dates were required for the modeling process,

with the selected dates being based on the trend in *Figure 33*. The first date chosen was 15 September 2017, which was due to the fact that this date exhibited a significant drop in impedance when compared to the 13 September 2017. The next date that was chosen was 20 September 2017 due to the fact that this date showed a value that was nearly double that of the previous two data sets. After this, the 27 September 2017 was chosen because, like 15 September, it exhibited a marked decrease in the measured impedance value when compared to the data set immediately preceding it. After the 27 September, the data set seemed to stabilize somewhat, at which point it was deemed that only two additional data sets were required: 20 November 2017, since that was the data set for SS2, and 16 October 2017, since this data set was in the middle of the data sets from the 27 September and the 20 November. All dates selected for the modeling, along with their residence day number and the impedance value at 0.1 Hz, are listed below in *Table 3*.

Date	Day #	Impedance (Ω)
4/28/2017	0	9.91E+03
5/27/2017	29	3.66E+03
6/16/2017	49	3.80E+03
9/13/2017	138	3.64E+03
9/15/2017	140	1.74E+03
9/18/2017	143	1.79E+03
9/20/2017	145	3.71E+03
9/27/2017	152	1.91E+03
10/2/2017	157	2.06E+03
10/4/2017	159	1.90E+03
10/6/2017	161	1.98E+03
10/11/2017	166	2.09E+03
10/16/2017	171	1.89E+03
10/18/2017	173	2.08E+03
10/21/2017	176	2.21E+03
10/30/2017	185	2.18E+03
11/1/2017	187	1.99E+03
11/15/2017	201	2.08E+03
11/20/2017	206	1.98E+03

Table 3: The impedance values of the SS2 system at 0.1 Hz, along with the date tested and the applicable residency day of each particular data point. The values in **GREEN** indicate the dates that were subjected to the PEIS data modeling, which is discussed in greater detail in the "Analysis and Discussion of Results" section.

With the dates selected, as shown in *Table 3*, the modeling process was started with the data sets from each of the selected dates being run through a 2RC, a 3RC, and a 4RC model. After each model was run, a fitment line was superimposed over the data points collected by the PEIS system. The PEIS system then calculated a goodness of fit value based on how close the superimposed line fit to the data points, with smaller values signifying a better fit to the data. An example of the graph fits from the PEIS software is seen below in *Figure 34*, along with the goodness of fit values for all dates that were subjected to the modeling process.

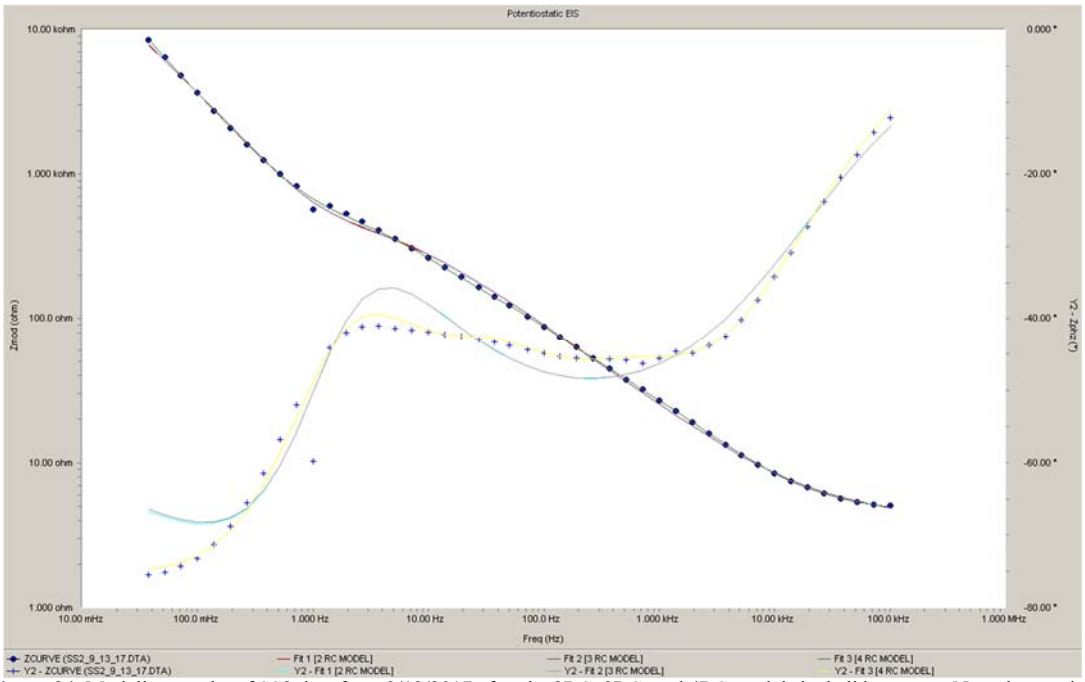

Figure 34: Modeling results of SS2 data from 9/13/2017 after the 2RC, 3RC, and 4RC models had all been run. Note the varying degrees of fit for each model. In this particular case, the 4RC model exhibited the best fit value. Additional graphs can be found in Appendix C.

Goodness of Fit – SS2	2 RC	3 RC	4 RC
4/28/2017	1.69E-04	1.81E-04	**8.14E-05**
5/27/2017	2.63E-03	**7.10E-04**	9.02E-04
6/16/2017	4.56E-03	2.15E-03	**1.66E-03**
9/13/2017	6.00E-03	6.08E-03	**1.93E-03**
9/15/2017	5.08E-04	1.67E-04	**1.55E-04**
9/20/2017	2.81E-03	6.20E-04	**2.95E-04**
9/27/2017	2.24E-04	2.22E-04	**2.16E-04**
10/16/2017	5.58E-04	1.59E-04	**1.33E-04**
11/20/2017	6.85E-04	**1.64E-04**	1.66E-04

Table 4: Goodness of fit values generated by the PEIS software for the selected SS2 data sets to analyze how close the generated line for each model came to fitting the actual data. The closer the value came to "0", the better the fit.

After analyzing the fitment data listed above in *Table 4*, it was determined that, overall, the best model fit for the majority of the data sets tested came from the 4RC model, which would indicate that four interfaces were present within the system as time progressed. The first sample date, 28 April 2017, indicated that there were four interfaces at play, which were theorized to be the following:

1. Stainless steel machine screw to the NaCl solution
2. CFRP panel surface to the NaCl solution
3. Stainless steel machine screw to the CFRP panel
4. Metal Oxide Layer to the NaCl solution

The presence of four interfaces would indicate that either an oxide formed extremely quickly on the surface of the stainless steel screw or a small oxide layer was already present on the screw. Interestingly, on the next data set dated 27 May 2017, the 3RC model showed the best fit. This would seem to indicate that one of the four interfaces, most likely the metal oxide to NaCl solution, was not in-play. This could potentially mean that the oxide layer that may have been previously been present had been broken down to the point when the Na^+ and Cl^- ions present in the salt water could directly attack the surface of the stainless steel screw. As the testing progressed, the system appeared to revert to the 4RC model, again based on the goodness of fit values calculated by the PEIS software, as shown in *Table 4*. This would seem to indicate that the oxide layer had reformed on the surface of the screw, thereby providing some measure of protection from the corrosive environment. The continued until the final data set dated 20 November, in which the 3RC and 4RC goodness of fit values were nearly identical, with the 3RC value being slightly lower. It is possible that this small shift indicated the beginning of the breakdown of the oxide layer that was providing nominal protection for the stainless steel screw surface.

CHAPTER 5

CONCLUSION

Over the course of the study, indications that CFRP could be damaged by the corrosion processes of either stainless steel or titanium were investigated. The results for titanium, both in the visual and numerical realms, indicated that titanium forms a stable corrosion product in salt water that both protects the titanium from further corrosion as well as preventing any mechanical damage to the CFRP that it is connected to. The stainless steel used in this study yielded different results. When connected to the CFRP in salt water, the stainless steel screw corroded more readily, exhibiting pitting corrosion and crevice corrosion mechanisms. In addition, the CFRP that had been connected to the stainless steel screw exhibited significantly more surface deformation than the titanium sample, with the primary surface deformation observed being delamination. Furthermore, products of the stainless steel corrosion process were found in abundance in and around the delaminated areas as well as within the threads of the CFRP. While this does not definitively prove that the stainless steel corrosion product damaged the CFRP, it lends credence to the hypothesis of the study. Further studies would be required to be able to prove whether or not stainless steel corrosion when connected to CFRP in a salt water environment can cause mechanical damage to the CFRP.

Based on the initial results of this experiment, the easy conclusion that could be reached would be to replace stainless steel components with titanium components. While this would in theory solve the corrosion issue, titanium on average is

significantly more expensive than common stainless steel, making this solution not economically viable for most applications. As such, it is recommended that further studies be performed, with some suggestions listed below.

RECOMMENDED FUTURE STUDIES

1. Test other types of CFRP in conjunction with other types of stainless steel. In the galvanic series table listed in this study (*Figure 1*), four different stainless steel types are listed, so it would be interesting to see how varying stainless steel grades react to be couples to a CFRP in a salt water medium. It would also be interesting to see if different types of CFRP type are more susceptible to mechanical damage from stainless steel corrosion, specifically when in conjunction with stainless steel grades that would more readily corrode.
2. In this study, titanium and stainless steel were investigated. It would be interesting to see how other commonly used metals, such as aluminum, would behave in similar settings and how the CFRP would react to those metals corroding.
3. Due to time constraints, the longest residence time possible in this experiment was 7 months. In order to get a more complete picture of the problem, a long term test using stainless steel coupled with CFRP with a residence of 1-2 years could provide a more complete picture of how CFRP reacts to stainless steel corrosion in salt water.
4. It would be recommended to run a similar test setup to what was performed in this study, but change the way the samples are visually inspected. Instead of removing the screw from the CFRP panel, keep the screw in the panel and mount the entire sample (screw and CFRP panel) into epoxy to stabilize it. Then carefully cut the sample in half and examine it using the SEM. It is possible that, when the screw was removed in this study, some evidence of mechanical damage could have been disturbed. This

sample analysis method may help to prevent or mitigate disturbance of the stainless steel/CFRP interface.

5. In this experiment, 3.5wt% salt water is used. The ions in this solution, Na^+ and Cl^-, are not the only present in natural seawater. It would be interesting to see how the results would differ if the samples were to be placed in artificial seawater and actual seawater.

APPENDIX A – OTHER PEIS MODELS USED

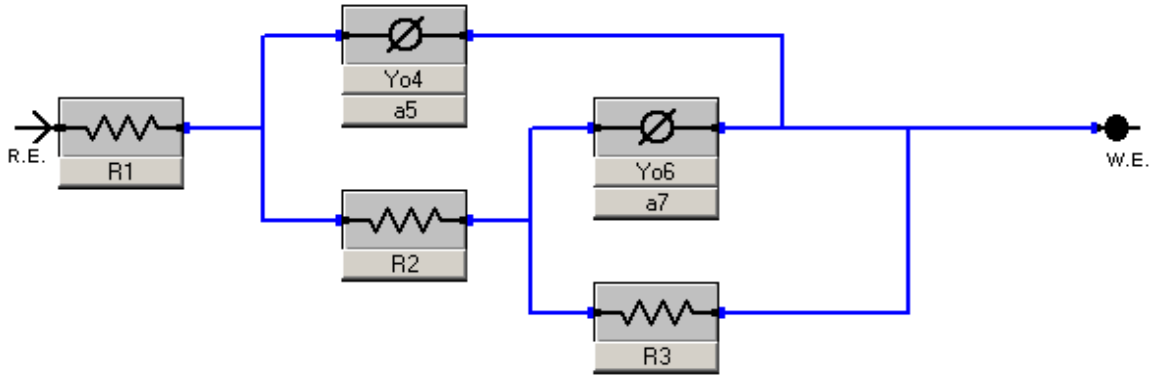

Figure 35: An example of one of the models used to analyze the data within the PEIS software, with this particular model containing 2 Randles Circuits. Each Randles Circuit consists of one resistor and one constant phase element.

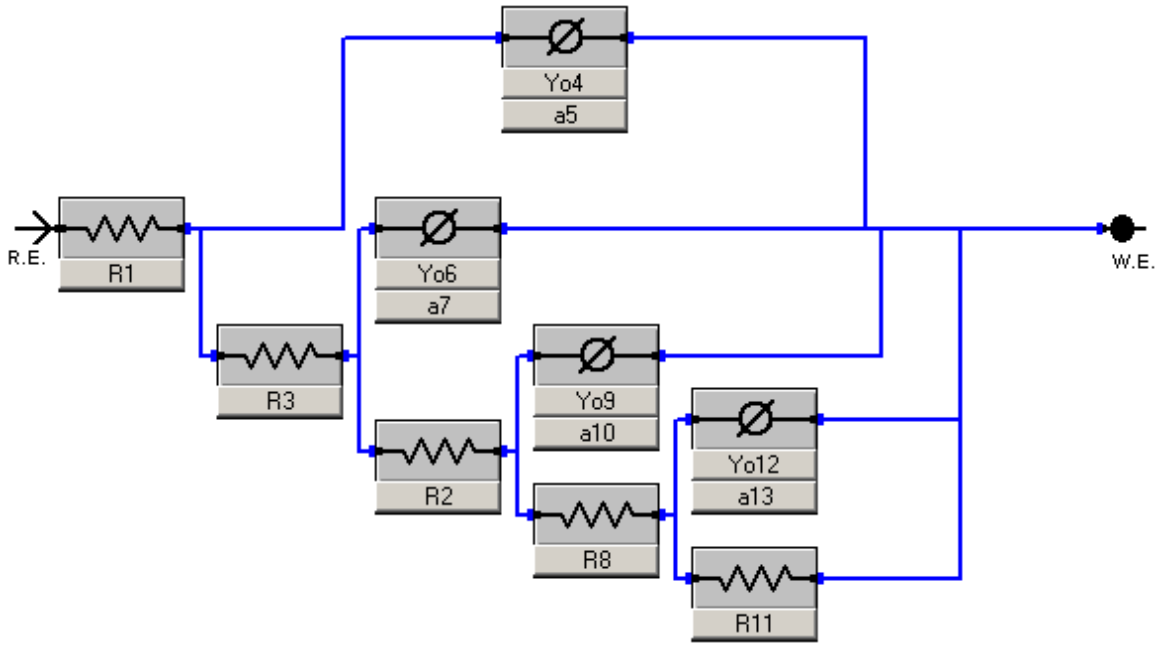

Figure 36: An example of one of the models used to analyze the data within the PEIS software, with this particular model containing 4 Randles Circuits. Each Randles Circuit consists of one resistor and one constant phase element.

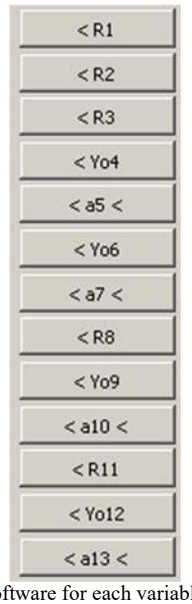

Figure 37: The image details the limits set in the software for each variable. The "R" and "Y_o" values were all given a lower limit of greater than 0, while the "a" values were given a limit of between 0 and 1. These limits were automatically set by the software.

APPENDIX B – PEIS MODELING FITMENT GRAPHS FOR TITANIUM "TI2"

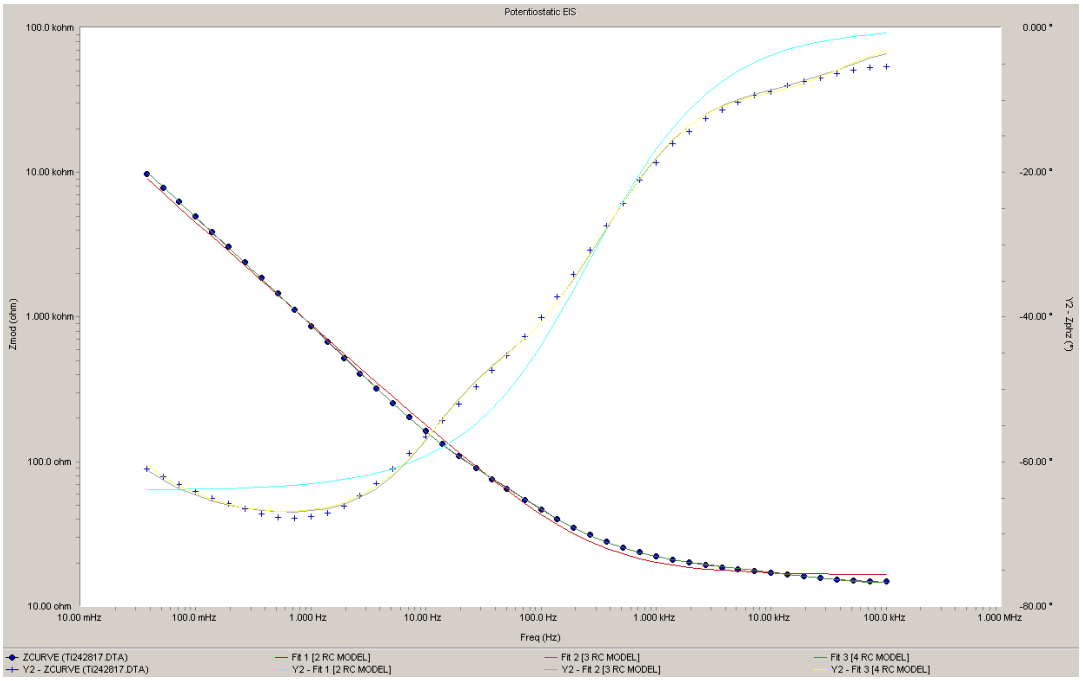

Figure 38: Modeling results of Ti2 data from 4/28/2017 after the 2RC, 3RC, and 4RC models had all been run.

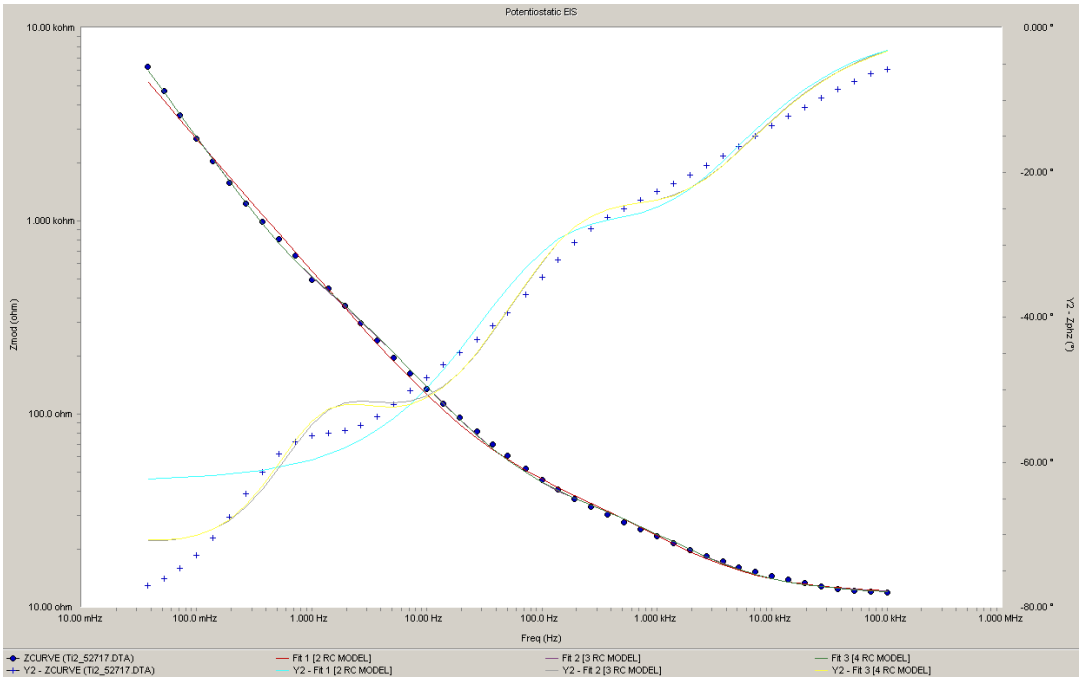

Figure 39: Modeling results of Ti2 data from 5/27/2017 after the 2RC, 3RC, and 4RC models had all been run.

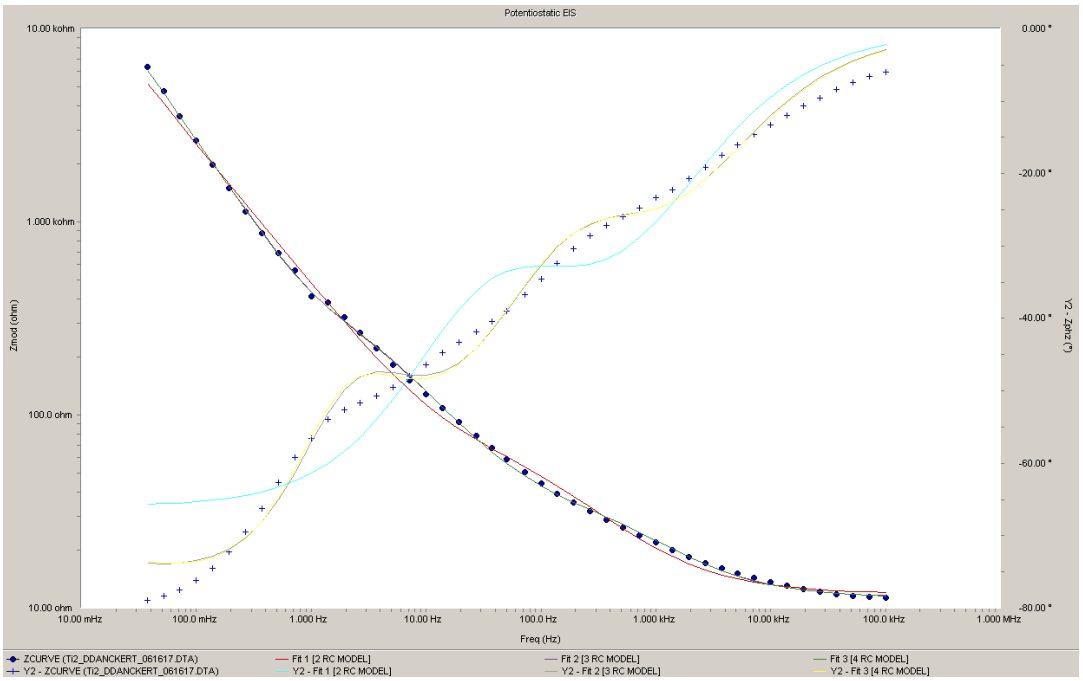

Figure 40: Modeling results of Ti2 data from 6/16/2017 after the 2RC, 3RC, and 4RC models had all been run.

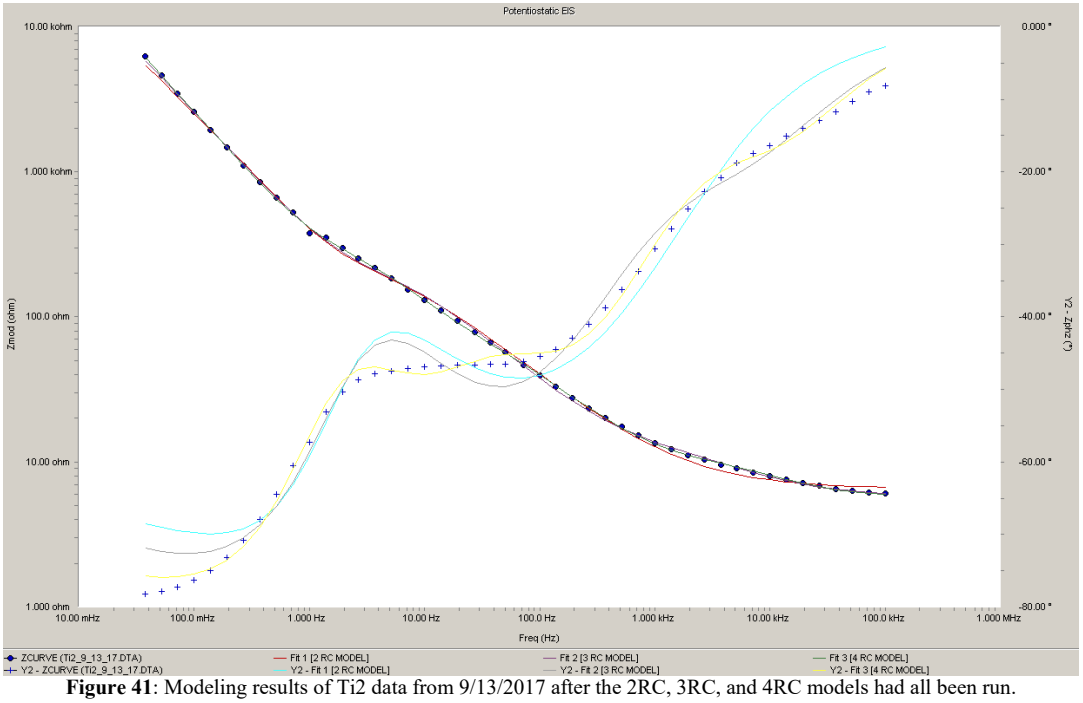

Figure 41: Modeling results of Ti2 data from 9/13/2017 after the 2RC, 3RC, and 4RC models had all been run.

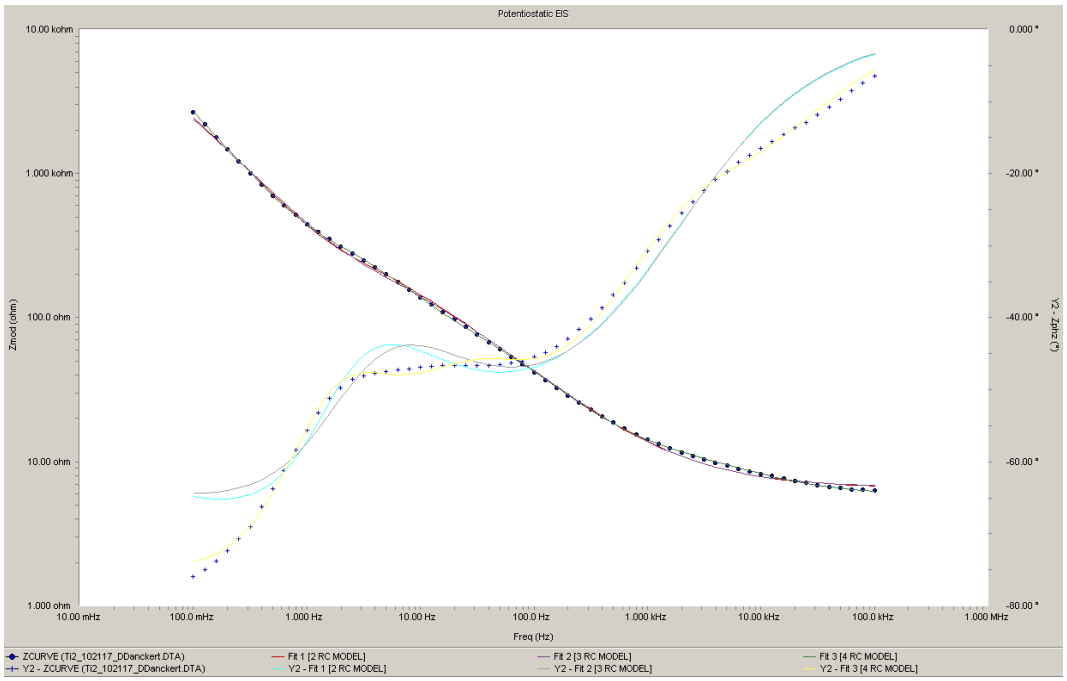

Figure 42: Modeling results of Ti2 data from 10/21/2017 after the 2RC, 3RC, and 4RC models had all been run.

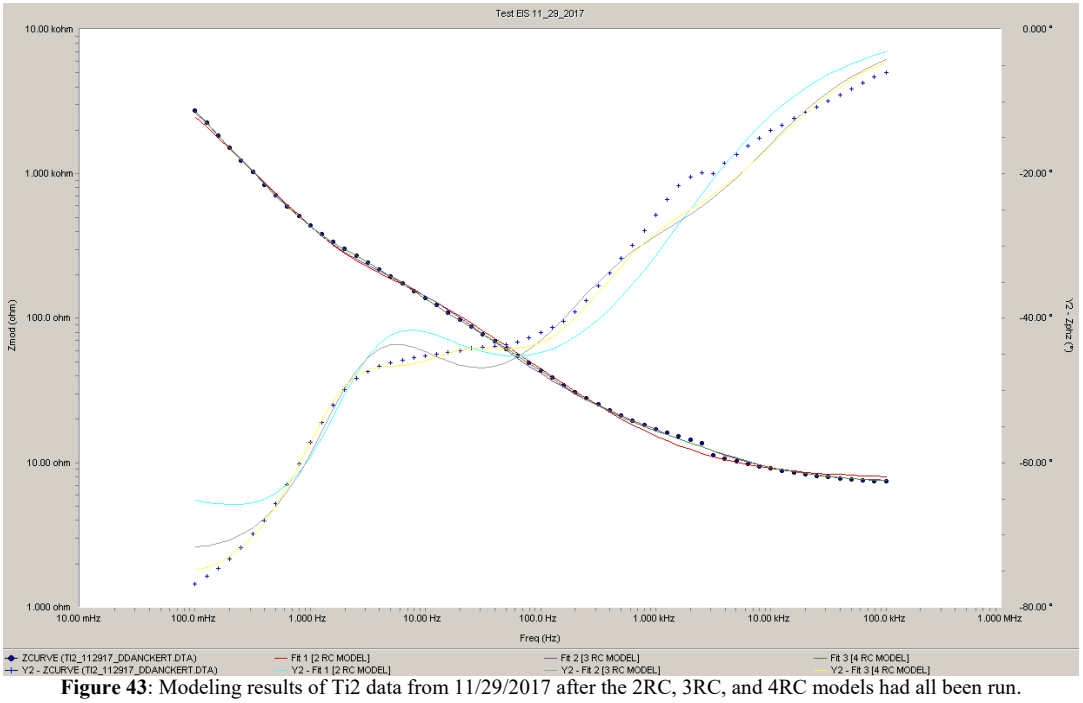

Figure 43: Modeling results of Ti2 data from 11/29/2017 after the 2RC, 3RC, and 4RC models had all been run.

APPENDIX C – PEIS MODELING FITMENT GRAPHS FOR STAINLESS STEEL "SS2"

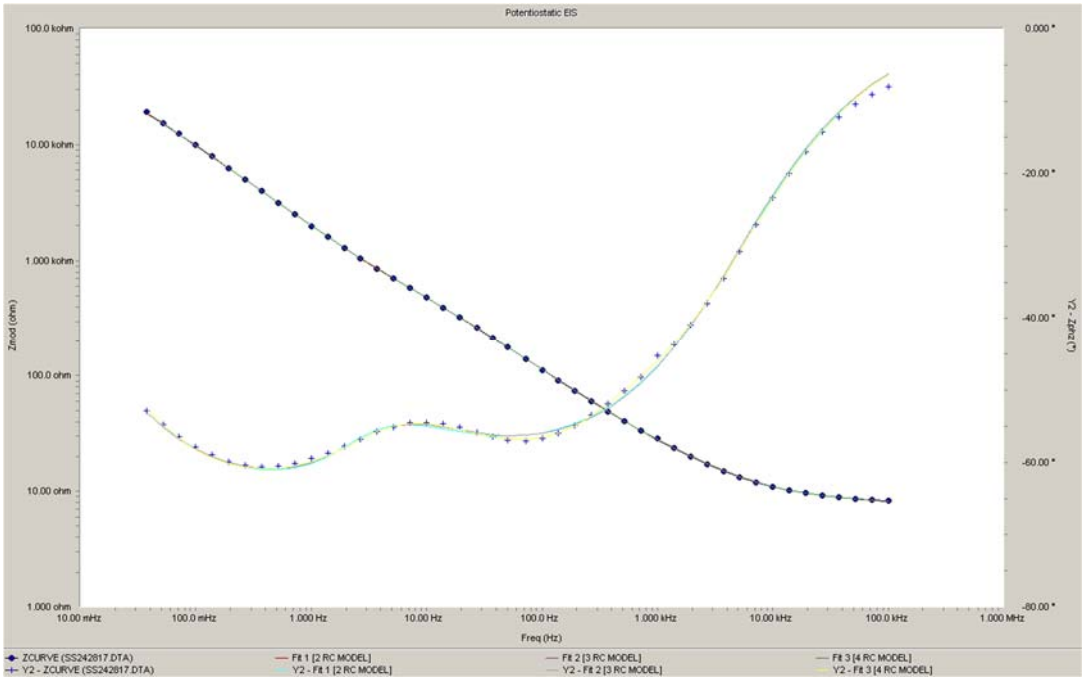

Figure 44: Modeling results of SS2 data from 4/28/2017 after the 2RC, 3RC, and 4RC models had all been run.

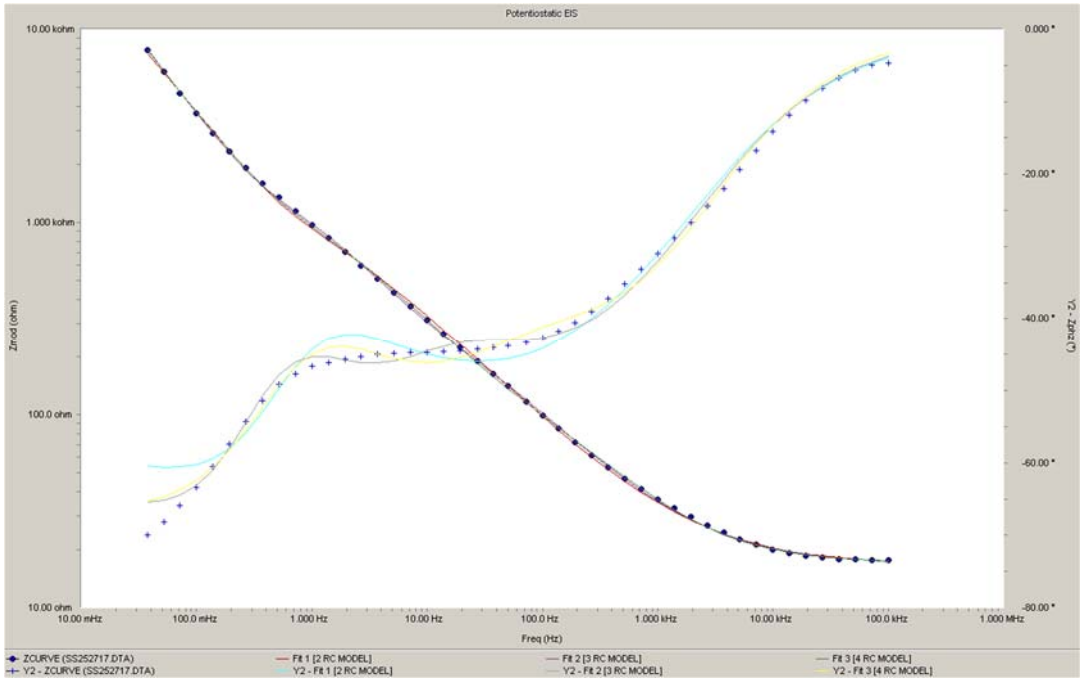

Figure 45: Modeling results of SS2 data from 5/27/2017 after the 2RC, 3RC, and 4RC models had all been run.

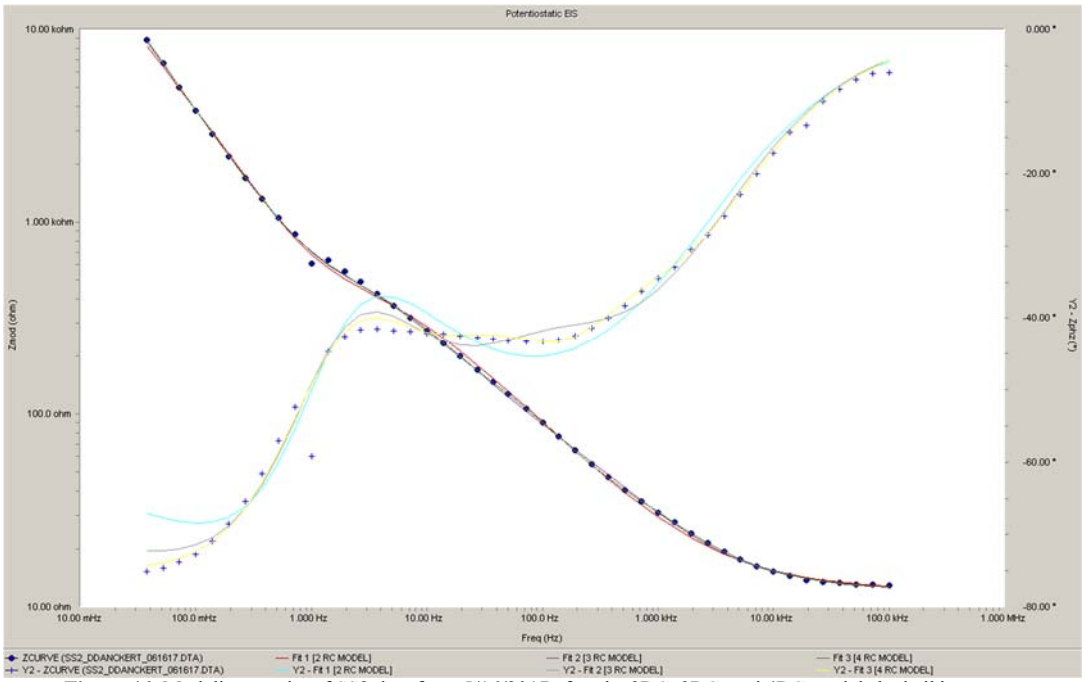

Figure 46: Modeling results of SS2 data from 5/16/2017 after the 2RC, 3RC, and 4RC models had all been run.

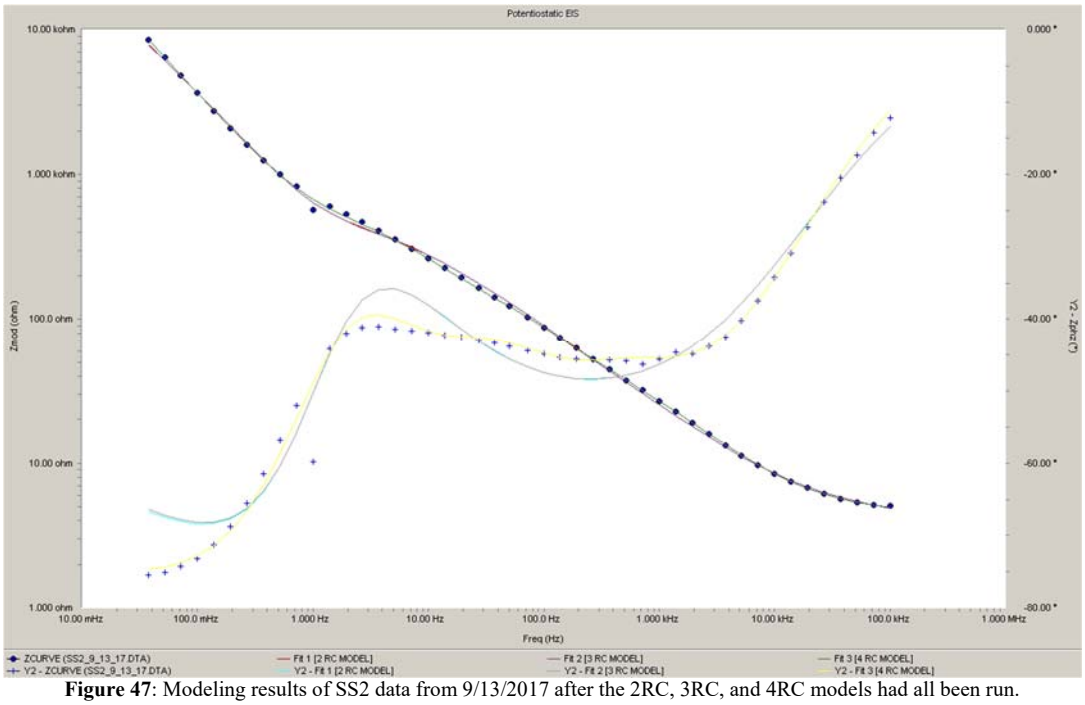

Figure 47: Modeling results of SS2 data from 9/13/2017 after the 2RC, 3RC, and 4RC models had all been run.

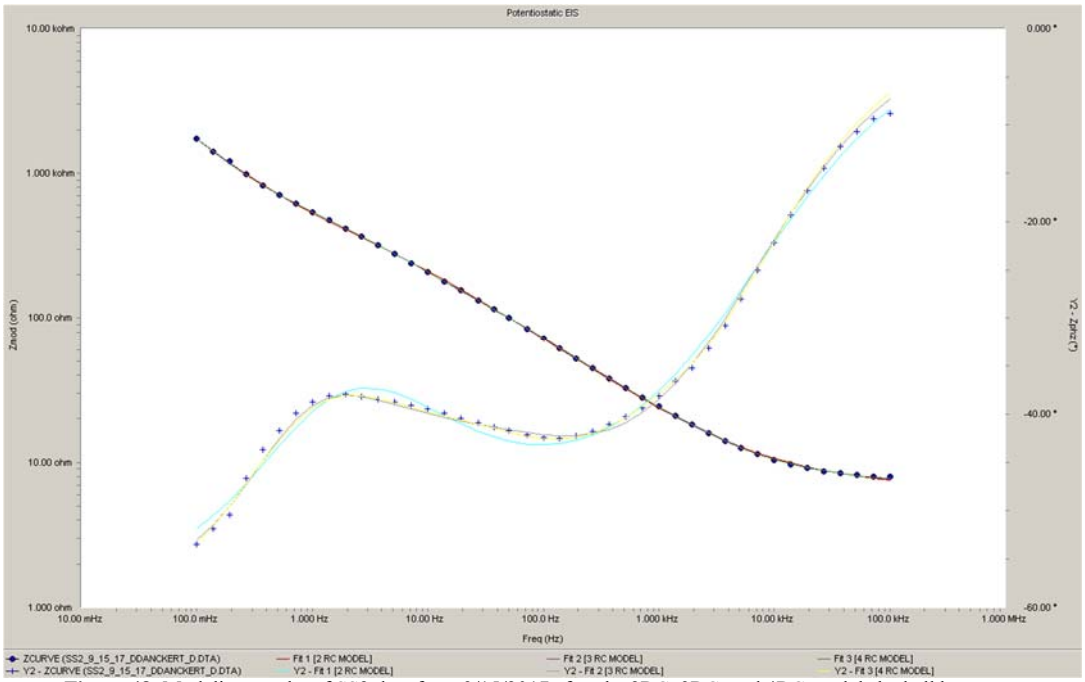

Figure 48: Modeling results of SS2 data from 9/15/2017 after the 2RC, 3RC, and 4RC models had all been run.

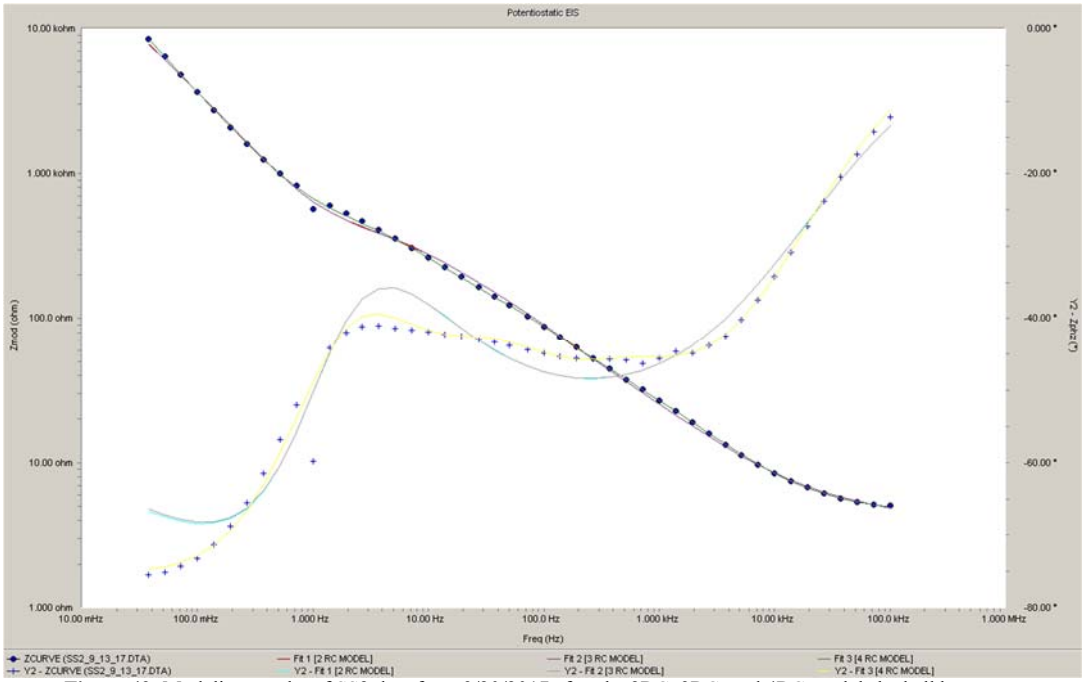

Figure 49: Modeling results of SS2 data from 9/20/2017 after the 2RC, 3RC, and 4RC models had all been run.

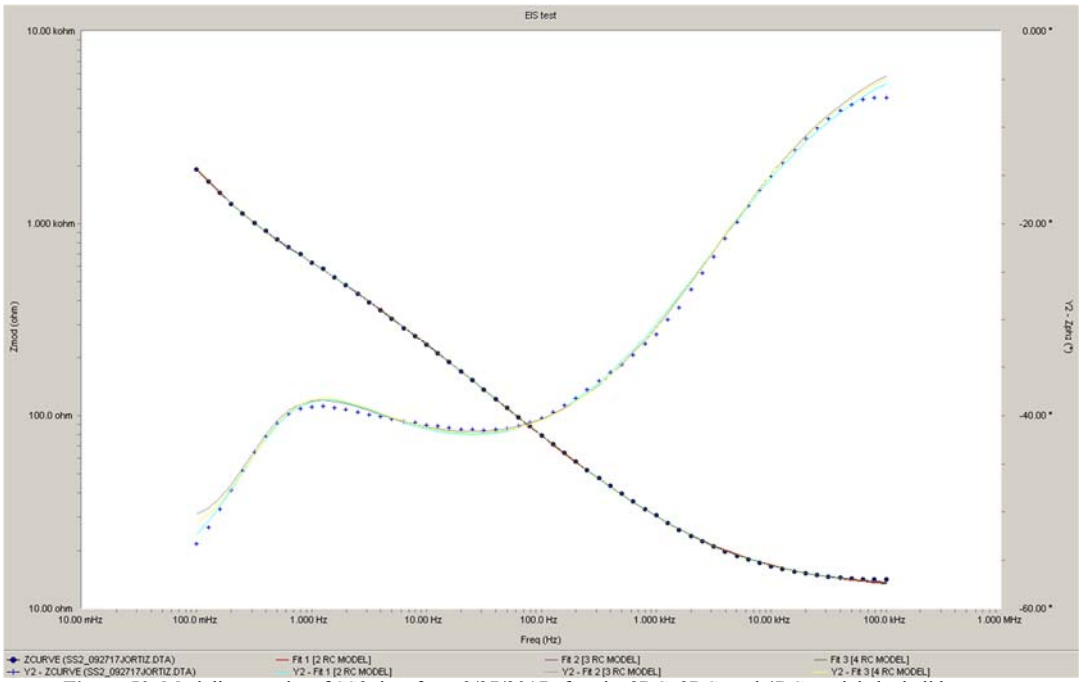

Figure 50: Modeling results of SS2 data from 9/27/2017 after the 2RC, 3RC, and 4RC models had all been run.

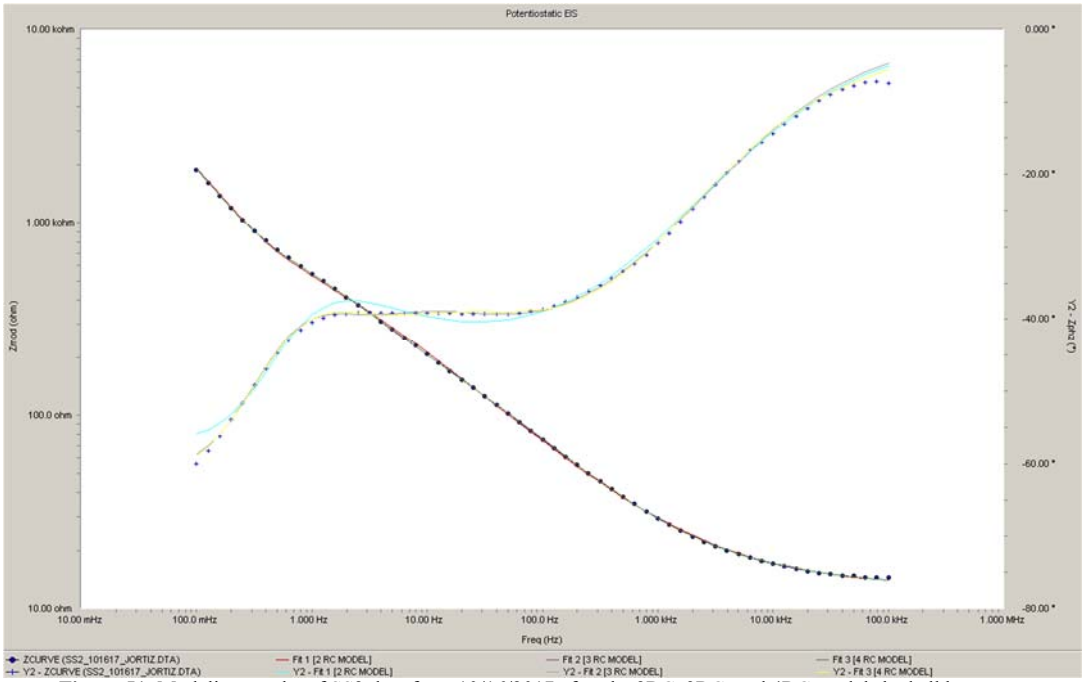

Figure 51: Modeling results of SS2 data from 10/16/2017 after the 2RC, 3RC, and 4RC models had all been run.

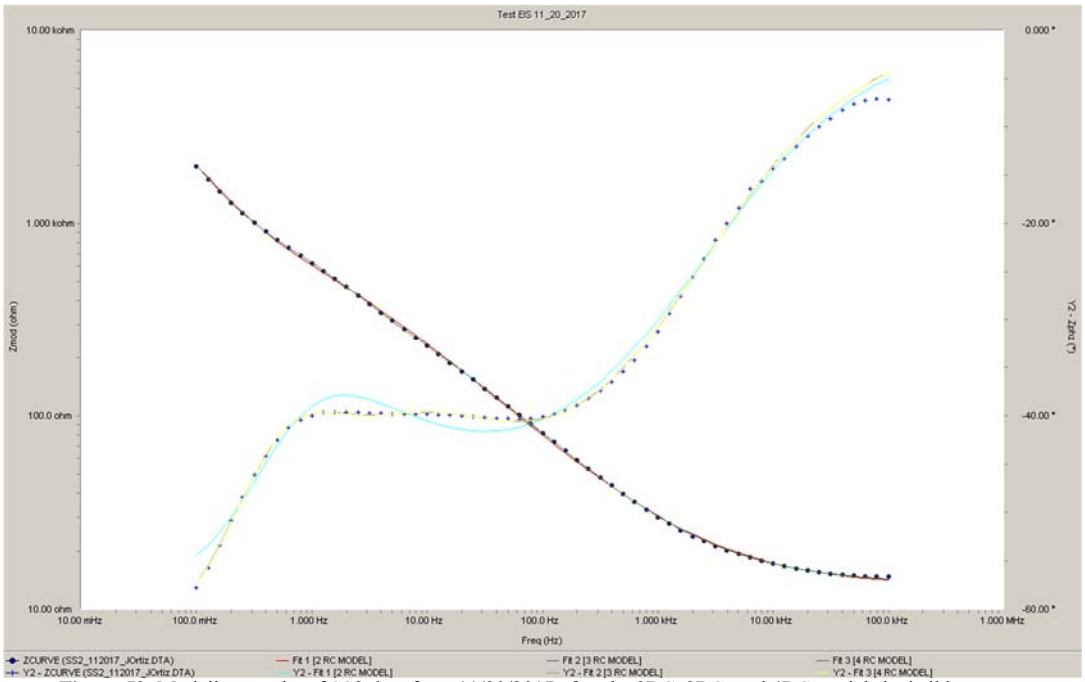

Figure 52: Modeling results of SS2 data from 11/20/2017 after the 2RC, 3RC, and 4RC models had all been run.

BIBLIOGRAPHY

Ahmad S, Malik AU. 2001. Corrosion behavior of some conventional and high alloy stainless steels in gulf seawater. J. Appl. Electrochem. 31:1009–1016. doi:10.1023/A:1017945713331.

Brown R, Reynolds WHE. 1995. The Effect of Various Chloride Environments on Degradation of a Carbon Fiber Composite. Corrosion:1–14.

Commander M. 1999. Carbon Fiber Composites for Marine Applications. Mater. World 7:403–405.

El-Dahshan ME, Shams El Din AM, Haggag HH. 2002. Galvanic corrosion in the systems titanium/316 L stainless steel/Al brass in Arabian Gulf water. Desalination 142:161–169. doi:10.1016/S0011-9164(01)00435-0.

Elsariti SM, Haftirman. 2013. Behaviour of Stress Corrosion Cracking of Austenitic Stainless Steels in Sodium Chloride Solutions. Procedia Eng. 53:650–654. doi:10.1016/j.proeng.2013.02.084.

Judy Jr. RW, Goode RJ. 1967. Stress-Corrosion Cracking Characteristics of Alloys of Titanium in Salt Water.

Lasia A. 1999. Electrochemical Impedance Spectroscopy and its Applications. Kluwer Acad. Publ. 32:143–248.

MacAnder A, Silvergleit M. 1977. Effects of Marine Environment on Stressed and Unstressed Graphite-Epoxy Composites. Nav. Eng. J. 89:65–72.

Park S, Yo J-S. 2003. Electrochemical Impedance Spectroscopy: For Better Electrochemical Measurements. Anal. Chem.:455–461.

Qin J, Brown R, Ghiorse S, Shuford R. 1995. The Effect of Carbon Fiber Type on the

Electrochemical Degradation of Carbon Fiber Polymer Composites.pdf. Corrosion:275/1-17.

Rebak RB. 2013. 2 Corrosion of Non-Ferrous Alloys . and Titanium-Based Alloys. In: Materials Science and Technology. p. 104–108.

Shindo D, Oikawa T. 2002. Energy Dispersive X-ray Spectroscopy. In: Analytical Electron Microscopy for Materials Science. Tokyo: Springer Japan. p. 81–102.

Smiderle J, Pardal JM, Tavares SSM, Vidal a. CN. 2014. Premature failure of superduplex stainless steel pipe by pitting in sea water environment. Eng. Fail. Anal. 46:134–139. doi:10.1016/j.engfailanal.2014.08.001.

SSINA KnowledgeBase. Corrosion: Galvanic Corrosion. Spec. Steel Ind. North Am.:1–4. [accessed 2018 Mar 2]. http://www.ssina.com/corrosion/galvanic.html.

Tsutsumi Y, Nishikata A, Tsuru T. 2007. Pitting corrosion mechanism of Type 304 stainless steel under a droplet of chloride solutions. Corros. Sci. 49:1394–1407. doi:10.1016/j.corsci.2006.08.016.

Tucker WC, Brown R. 1989. Blister Formation on Graphite / Polymer Composites Galvanically Coupled with Steel in Seawater. J. Compos. Mater. 23:389–395. doi:10.1177/002199838902300406.

Tucker WC, Brown R, Russell L. 1990. Corrosion Between a Graphite/Polymer Composite and Metals. J. Compos. Mater. 24:92–102.